

Bayesian Statistical Inversion for High-Dimensional Computer Model Output and Spatially Distributed Counts

Steven D. Barnett* Robert B. Gramacy† Lauren J. Beesley‡
 Dave Osthus‡ Yifan Huang§ Fan Guo¶ Daniel B. Reisenfeld||

Abstract

Data collected by the Interstellar Boundary Explorer (IBEX) satellite, recording heliospheric energetic neutral atoms (ENAs), exhibit a phenomenon that has caused space scientists to revise hypotheses about the physical processes, and computer simulations under those models, in play at the boundary of our solar system. Evaluating the fit of these computer models involves tuning their parameters to observational data from IBEX. This would be a classic (Bayesian) inverse problem if not for three challenges: (1) the computer simulations are slow, limiting the size of campaigns of runs; so (2) surrogate modeling is essential, but outputs are high-resolution images, thwarting conventional methods; and (3) IBEX observations are counts, whereas most inverse problem techniques assume Gaussian field data. To fill that gap we propose a novel approach to Bayesian inverse problems coupling a Poisson response with a sparse Gaussian process surrogate using the Vecchia approximation. We demonstrate the capabilities of our proposed framework, which compare favorably to alternatives, through multiple simulated examples in terms of recovering “true” computer model parameters and accurate out-of-sample prediction. We then apply this new technology to IBEX satellite data and associated computer models developed at Los Alamos National Laboratory.

Key words: Gaussian process, surrogate modeling, Poisson, calibration, heliospheric science, IBEX, Vecchia approximation

1 Introduction

The National Aeronautics and Space Administration (NASA) launched the Interstellar Boundary Explorer (IBEX) satellite in 2008 as part of their Small Explorer program (McComas et al., 2009) to deepen our understanding of the heliosphere. The heliosphere is the bubble formed by the solar

*Corresponding author sdbarnett@vt.edu, Department of Statistics, Virginia Tech

†Department of Statistics, Virginia Tech

‡Statistics Group, Los Alamos National Laboratory

§Center for Space Plasma and Aeronomic Research, University of Alabama in Huntsville

¶Nuclear and Particle Physics, AstroPhysics and Cosmology, Los Alamos National Laboratory

||Space Science and Applications Group, Los Alamos National Laboratory

wind that encompasses our solar system and acts as a barrier to interstellar space. Of particular interest is the behavior at the edge of the heliosphere. Here, highly energized hydrogen ions that make up the solar wind interact with neutral atoms, occasionally undergo electron exchange, and become neutral themselves. These energetic neutral atoms (ENAs) are unaffected by magnetic fields and therefore travel in a ballistic trajectory.

Some ENAs eventually make their way to Earth and can be detected by an instrument on the IBEX satellite called the IBEX-Hi ENA imager (Funsten et al., 2009). This apparatus records the energy level and approximate location of origin for each ENA that enters the detector. IBEX’s raw collected data consist of ENA counts and exposure times for each area of the sky at which the satellite points, providing sufficient information to estimate the rate at which these particles are created throughout the heliosphere. An example of the observed ENA rates detected by the IBEX satellite used to make *sky maps* (spatial maps of heliospheric ENA rates) can be found in the left panel of Figure 1. Sky maps are integral to better understand the heliosphere’s properties and evolution.

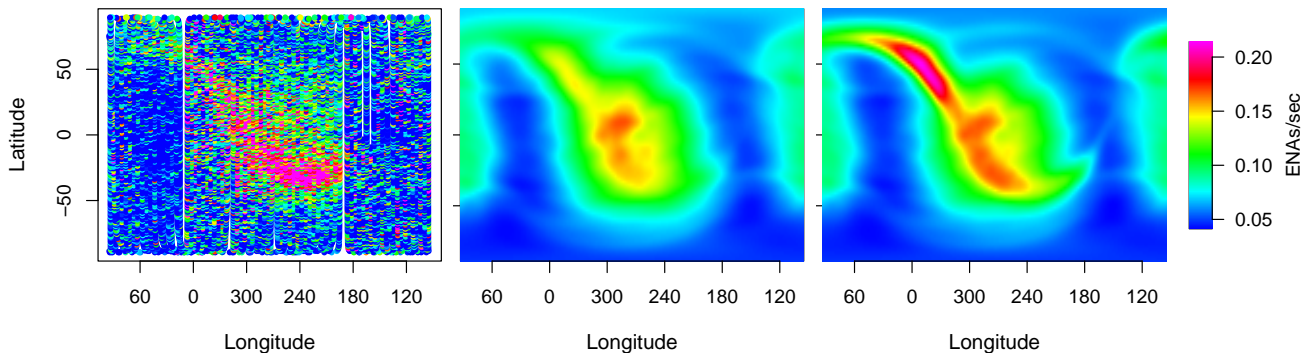


Figure 1: Observed ENA rates detected by the IBEX satellite (left) and output from two IBEX simulations under different parameter settings (middle, right).

One can think of the heliosphere as a “boat” moving through interstellar space. At the outset of IBEX’s mission, scientists expected to see ENAs being generated throughout the heliosphere, with elevated rates at the front (nose) and back (tail), much like the turbulent interaction with water at a boat’s bow and stern. And indeed, that belief was validated by IBEX data. At the nose and tail of the heliosphere IBEX observed an increased number of collisions and resulting electron exchanges between hydrogen ions and neutral particles. These sources of ENAs, originating from the heliosheath (region between the termination shock and the edge of the heliosphere), are identified as *globally distributed flux*, or GDF.

However, in a completely unanticipated finding, IBEX also recorded a thin string of higher rates of ENAs (Fuselier et al., 2009) wrapping around the heliosphere. Scientists now refer to this phenomenon as the *ribbon*. This unique feature of a sky map is clearly visible in Fig. 1. Since this discovery, space scientists have proposed several theories attempting to describe the physical process that generates the ribbon (McComas et al., 2014; Zirnstein et al., 2018, 2019, 2021a).

Computer models encapsulating competing theories have been built, which generate high-resolution (i.e, a high-dimensional response) synthetic sky maps (middle and right panels of Figure 1). These

simulations are extremely sophisticated and involve many complex and expensive operations (e.g. solving differential equations). Consequently, executing a single run of the computer model at a specified set of model parameters can take hours, even when leveraging parallel processing. This severely limits the number of unique runs available to generate simulated sky maps in various settings.

Our work here focuses on two computer models provided to us by heliospheric physicists involved in IBEX’s mission: a GDF model proposed by Zirnstein et al. (2021b, 2025); Swaczyna et al. (2020); and a ribbon-only model developed by Huang et al. (2025). These simulators take inputs that can be varied to modify either the GDF or the shape and intensity of the ribbon. The ribbon-only model relies on two parameters of interest, *parallel mean free path* and *ratio*, while we fix the GDF model as constant and simply add its response to the output of the ribbon model. Dialing in good settings for these input parameters, in light of observed ENA counts from IBEX, is instrumental in furthering theory development and validation.

Space scientists at Los Alamos National Laboratory (LANL) want to know which parameter settings best agree with IBEX observations. One way to do this is to treat the problem as a Bayesian inverse problem (Kaipio and Fox, 2011; Stuart, 2010; Knapik et al., 2011), obtaining a posterior distribution over likely settings. However, the exposure and count data IBEX provides, along with computer simulated rates, present some unique challenges: 1) computationally intensive models limiting simulation, necessitating surrogate modeling; 2) high-dimensional model output (simulated sky maps, each containing tens of thousands of pixels), thwarting conventional surrogate modeling techniques; and 3) a non-Gaussian field response (Poisson counts). It is worth noting that Bayesian posterior sampling, say via Markov chain Monte Carlo (MCMC), compounds computational bottlenecks (2). We propose a framework for Bayesian inverse problems that utilizes the Vecchia approximation (Katzfuss and Guinness, 2021; Katzfuss et al., 2022) with a Gaussian process (GP) surrogate or emulator for high-dimensional computer simulations, and couple that with a Poisson observational model to furnish posterior samples of unknown parameters to these models given observed data.

Methods exist separately, in the literature, to address needs in each of the aforementioned situations 1)–3), but we are not aware of any approaches in the intersection. Table 1 summarizes the features of the IBEX inverse problem and reviews the necessary capabilities, alongside recent papers offering partial solutions. References provided are representative. We acknowledge that there are, in most cases, several works that may fit the bill. Each row in the table may be summarized as follows.

Kennedy and O’Hagan (2001) offer the canonical computer model calibration framework, which provides a fully Bayesian approach to estimate the posterior distribution of model parameters and improve prediction at new, unobserved field locations. However, their methodology is limited to Gaussian field observations and small, simulator output. Higdon et al. (2008) and SEPIA (Gattiker et al., 2020), its more recent incarnation, also employ Bayesian methods while accounting for computer model output that is functional. But SEPIA is somewhat rigid, only considers Gaussian field observations, does not scale well with added model runs, and requires the user to specify a number of basis functions to represent the simulator response. Gramacy et al. (2015) consider computer model calibration with large-scale output from a computer experiment, necessitating an approximation. But their implementation is not Bayesian and the scale of simulator data is still orders of magnitude

	Bayesian	Non-Gaussian	Large-Scale Simulation Output	High-Dim Response
Our Contribution	✓	✓	✓	✓
Kennedy and O’Hagan (2001)	✓			
Higdon et al. (2008)	✓			✓
Gramacy et al. (2015)			✓	
Grosskopf et al. (2020)	✓	✓		

Table 1: Check marks indicate that functionality exists within the cited paper and/or accompanying software. To save space, only one citation is listed for each row.

less than IBEX. Grosskopf et al. (2020) provide an extension of the Kennedy & O’Hagan (hereafter referred to as KOH) framework to non-Gaussian data that maintains a Bayesian approach. But they are limited to small amounts of computer model data and do not consider higher dimensional responses. In contrast, our approach checks all the boxes to achieve the goal of IBEX space scientists and therefore applies to a wider class of problems than previous work.

Our integrated framework for Bayesian inverse problems overcomes these obstacles together in an all-in-one solution, as illustrated in the top row of Table 1. We adopt the approach of generalized computer model calibration, adapting to IBEX’s count data with a Poisson likelihood and employing MCMC to garner posterior samples of model parameters, which determine the underlying mean of our Poisson model, given observed data. These samples allow us to estimate the full joint posterior distribution of the unknown parameters. We access predicted ENA rates through a GP surrogate or emulator fit to a limited set of expensive, high-dimensional IBEX computer simulations to more thoroughly explore the domain of possible sky maps that serves as the basis for the observed ENA counts. As previously stated, MCMC exacerbates the computational burden of making surrogate predictions, necessitating not only a sparse GP surrogate, but one that can swiftly generate repeated sky map proposals at each MCMC iteration. We find the Vecchia approximation to be extremely effective in this regard. Lastly, we propose a more intuitive technique to modeling high-dimensional vectors, treating each pixel representing an ENA rate as a scalar response of interest. This differs from previous approaches to functional computer model output, but enables us to leverage recent advances in sparse GP surrogate modeling. Additionally, using this strategy efficiently scales both to increased dimensionality of the response and to larger sizes of training sets.

Our paper is laid out as follows. First, Section 2 reviews methods that form the foundation for our work, namely Bayesian inverse problems and Gaussian process surrogate models, and introduces our framework for solving the inverse problem in the context of non-Gaussian field observations. We also give a brief description of the methodology and implementation behind SEPIA, the current “status quo” in Bayesian inverse problems for high-dimensional computer model output. Section 3 describes our use of the Vecchia approximation to stretch the capacity of a GP surrogate beyond small simulator training runs. In Section 4 we return to our motivating application, illustrating the effectiveness of our framework in discovering the true, underlying model parameters on synthetic

data and apply our methods to the raw IBEX satellite data. To conclude, we discuss any extensions and future work in Section 5. Our implementation may be found at <https://github.com/lanl/ibex-bayesian-inverse> along with code reproducing all included examples.

2 Bayesian inverse problems

We study IBEX through the lens of observational data Y^F (F for field measurement) and a computer implementation of a physical model $m(u, X)$, where parameters u are unknown and X represents the spatial locations where the simulation output is evaluated. These may be the locations X^F that correspond to field measurements Y^F , or a grid of predictive locations supporting high resolution visuals. Given prior information about u , we want to know which u 's lead to realizations of $m(\cdot, \cdot)$ that could explain Y^F , i.e., the posterior for $u \mid Y^F$.

This is a classic Bayesian inverse problem (Kaipio and Fox, 2011; Stuart, 2010; Knapik et al., 2011). Eq. 1 provides the typical hierarchical model used in this setting, generally with Gaussian field data Y^F .

$$\begin{aligned}
 Y^F &\sim \mathcal{N}_{n_F}(\mu(X^F), \Sigma(X^F)) \\
 \mu(X) &= m(u, X) \\
 \Sigma(X) &\sim \pi(\Sigma) && \text{e.g., } \Sigma^{-1} \sim \text{Wishart}((\rho V)^{-1}, \rho) \\
 u &\sim \pi(u) && \text{e.g., } u \sim \text{Unif}[0, 1]^p
 \end{aligned} \tag{1}$$

One big difference with Bayesian inverse problems, as opposed to ordinary Bayesian inference, is that the parameters $\mu(X^F)$ and $\Sigma(X^F)$ defining the distribution of Y^F are not of direct interest. Rather, we are interested in settings u that define $\mu(X)$ and $\Sigma(X)$ through $m(u, X)$. For example, two different settings of u were used in the IBEX simulator to generate the center and right panels of Figure 1. Colors indicate output $\mu(X)$ values on a dense grid X of longitudes and latitudes. We are interested in learning which u are likely to have generated the recorded Y^F values in the left panel, observed at locations where the IBEX satellite was pointed (X^F) to collect ENAs.

To help fix ideas, consider the simpler example introduced in the left panel of Figure 2. Red stars indicate noisy field measurements, Y^F , observed in replicate as $y_i \stackrel{\text{iid}}{\sim} \mathcal{N}(m(u^*, x_i), \sigma^2)$ for a “true” unknown $u^* = (u_1^*, u_2^*)^\top$ and uniform $x_i \in X^F$. In this simple example, the computer model $m(\cdot, \cdot)$ was used to generate the data. In practice, the model represents a caricature using known or best-guess physics. Each light gray line is a realization of $m(\cdot, \cdot)$ for a different u on a fine grid of spatial locations X . The bold-black-dashed line is $m(u^*, X)$ provided as a reference.

The middle panel of the figure shows runs of our virtual model evaluated at posterior draws of u obtained under Metropolis sampling using a multivariate normal likelihood whose mean $\mu(X^F) = m(u^{(t)}, X^F)$ and whose covariance $\Sigma(X^F) \sim \sigma^2 \mathbb{I}$, where σ^2 is marginalized out under a reference prior $\pi(\sigma^2) \propto 1/\sigma^2$. Although we display these runs on a high-resolution grid X , the sampler only uses evaluations of $m(u^{(t)}, X^F)$ in likelihood evaluations. The posterior samples of u thus obtained are shown in the right panel of the figure. In this toy example, it is evident that the Metropolis sampler successfully concentrates posterior mass around the true value of u .

The literature on Bayesian inverse problems involves methods that work predominantly in this way, particularly as regards a Gaussian likelihood. We aim to provide a method that achieves the

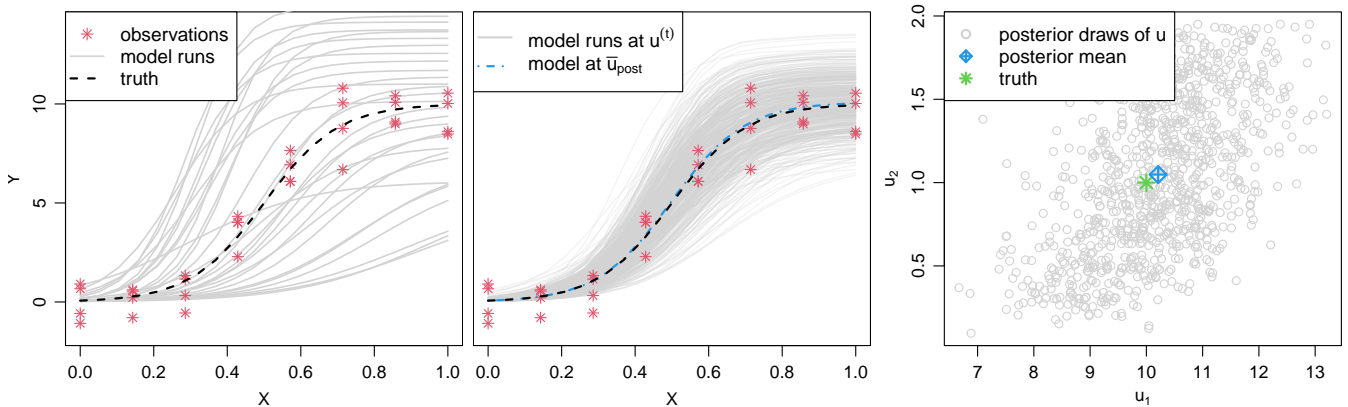


Figure 2: A simple inverse problem. Field observations and a small sample of computer model runs (left), model evaluations at posterior draws and mean (middle), and posterior distribution of model parameters (right).

same goal, but for unknown parameters u that underlie observed IBEX satellite data (left panel of Figure 1), whose observations are counts under variable exposure. Our first contribution, which is albeit rather straightforward, is to depart from that literature by using a Poisson likelihood.

2.1 Generalized Bayesian inverse problems

Our IBEX observations Y^F are counts under exposure $e(X^F)$, which is at odds with the canonical Gaussian likelihood in the Bayesian inverse problem setup introduced earlier. We wish to model a count $y \sim \text{Pois}(\lambda, e)$ where $f(y|\lambda, e) = \frac{(\lambda e)^y \exp\{-\lambda e\}}{y!}$ and $E(y) = \lambda e$. We thereby extend Eq. (1) as follows:

$$\begin{aligned}
 Y^F &\sim \text{Pois}(\lambda(X^F), e(X^F)) & \lambda(X) &= m(u, X) \\
 u &\sim \pi(u) & \text{e.g., } u &\sim \text{Unif}[0, 1]^p,
 \end{aligned}
 \tag{2}$$

where $e(X^F)$ represents the duration (in seconds) the satellite points at specific locations in the sky. $\lambda(X^F)$ denotes the rate at which ENA particles are generated for rows (latitude/longitude pairs) in X^F . Sampling from the posterior could proceed via Metropolis as in Algorithm 1. For the IBEX field data, we evaluate a Poisson likelihood given an exposure time for each observation and a mean surface determined by a simulator $m(\cdot, \cdot)$ at proposed values of u , although we believe it would be straightforward to accommodate other observational models.

Using Algorithm 1, we can build on the toy problem we introduced in Figure 2 and align it more closely with the IBEX data. Instead of observing a mean process $\mu(X^F)$ with random, Gaussian noise, suppose we are given counts, drawn from a Poisson process with $\lambda(X^F) = m(u^*, X^F)$, as shown in the left panel of Figure 3. Computer model runs $m(\cdot, \cdot) = \lambda(X)$ produce different mean surfaces given unique values of $u = (u_1, u_2)$. Observed counts are shown as red stars. Red circles

Algorithm 1: MCMC (Metropolis-within-Gibbs) for Poisson Bayesian inverse problems

 Initialize $u^{(0)}$.

 Set $\lambda(X^F)^{(0)} = m(u^{(0)}, X^F)$.

 Compute and store $\mathcal{L}(Y^F | \lambda(X^F)^{(0)}, e(X^F)) = \prod_{i=1}^{n_F} f(y_i | \lambda_i(X^F)^{(0)}, e_i)$,

for $t = 1, \dots, T$ **do**

 Propose new model parameters: $u^{(t)} \sim q(u^{(t)} | u^{(t-1)})$,

 Evaluate simulator at field locations and $u^{(t)}$: $\lambda(X^F)^{(t)} = m(u^{(t)}, X^F)$,

 Calculate and save $\mathcal{L}(Y^F | \lambda(X^F)^{(t)}, e(X^F)) = \prod_{i=1}^{n_F} f(y_i | \lambda_i(X^F)^{(t)}, e_i)$,

 Compute the acceptance ratio: $\alpha = \frac{\mathcal{L}(Y^F | \lambda(X^F)^{(t)}, e(X^F)) \pi(u^{(t)}) q(u^{(t-1)} | u^{(t)})}{\mathcal{L}(Y^F | \lambda(X^F)^{(t-1)}, e(X^F)) \pi(u^{(t-1)}) q(u^{(t)} | u^{(t-1)})}$,

 Accept or reject $u^{(t)}$.

indicate the sum of all counts at one input location (i.e, a single row of X^F) divided by the sum of their corresponding exposure times $e(\cdot)$. These points are the actual data we receive. Results from running Algorithm 1 are shown in the middle and right panels of Figure 3. Similar to the results in Figure 2, it is clear that the sampler searches a broad swath of the model input space but hones in on the region where the true parameter value lies.

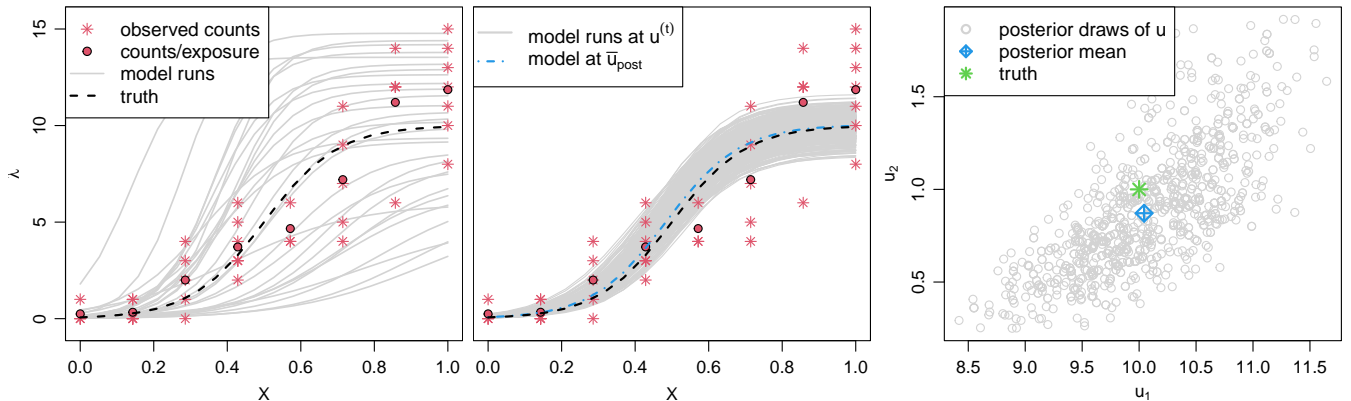


Figure 3: An inverse problem for a Poisson process. Counts observed in the field and a sample of computer model runs (left), model evaluations at posterior draws and mean (middle), and posterior distribution of model parameters (right).

In each of these toy examples we have made the assumption that we have unlimited access to simulator runs (i.e, for each proposed combination of model parameters, we can quickly get a response from the computer simulation). But that is rarely the case, presenting another challenge to the typical Bayesian inverse problem apparatus. For instance, each run of the IBEX model $m(\cdot, \cdot)$ is a real challenge, requiring hours, even when evaluated on a supercomputer. That simply cannot be embedded in a Metropolis sampler requiring thousands of iterations to converge. While

it’s rather conventional to deploy a surrogate model (e.g. Gramacy, 2020) in this setting, trained on a design of space-filling u -values, doing so effectively is challenged by the number of rows (i.e. unique measurement locations) in X^F . We considered multiple surrogate models developed to accomodate such scenarios (e.g. GPs via inducing points (Banerjee et al., 2008), local approximate GPs (Gramacy and Sun, 2014)), but found them unable to manage the scale of the IBEX data. Herein lies our main methodological contribution, using a modern sparse approach to surrogate modeling in a (Poisson) Bayesian inverse problem setting. The remainder of this section outlines the standard surrogate modeling toolkit, as a jumping-off point toward explaining both our main comparative (Section 2.3) and our main methodological contribution.

2.2 Gaussian process surrogates for computer experiments

Evaluating the likelihood Y_F in Algorithm 1 may proceed via surrogate when *in situ* evaluation directly on $m(\cdot, \cdot)$ is too slow. Suppose we have a vector of observations Y^M (M for computer model) at input locations X^M from a campaign of runs of $m(\cdot, \cdot)$ that may or may not coincide with settings in X^F . We prefer a small design of space-filling u -values (U), paired via Cartesian product with X^F from the field experiment or a predictive grid X , e.g., $X^M = X \otimes U$, depending on the situation. Two such runs, i.e., for two rows $u^\top \in U$ and a dense grid X , are shown in Figure 1.

Given a corpus of runs (Y^M, X^M) , a surrogate synthesizes this information in order to extend it to new inputs. Many surrogates for computer simulations are based on Gaussian processes (e.g., Rasmussen, 2003), where modeling boils down to specifying a multivariate normal (MVN) for all responses. This way, prediction is simply a matter of MVN conditioning rules, or *kriging* (Matheron, 1963), to derive the distribution of unknown (testing) output given known (training) values. Specifically, let $Y^M \sim \mathcal{N}_{n_M}(\mu(X^M), \Sigma(X^M))$, where \mathcal{N}_{n_M} indicates an n_M -variate MVN. Then, predicting at a new location x (think proposed u -value and paired row in X^F) follows $Y(x) | Y(X^M) \sim \mathcal{N}(\hat{\mu}(x), \hat{\sigma}^2(x))$, where

$$\begin{aligned}\hat{\mu}(x) &= \mu(x) + \Sigma(x, X^M)\Sigma(X^M)^{-1}(Y^M - \mu(X^M)) \\ \hat{\sigma}^2(x) &= \Sigma(x, x) - \Sigma(x, X^M)\Sigma(X^M)^{-1}\Sigma(X^M, x).\end{aligned}\tag{3}$$

Although a generic mean function is specified in Eq. (3), it is common to set $\mu(\cdot) = 0$ assuming pre-centered responses. In this zero-mean context, all the action takes place in the covariance function $\Sigma(x, x')$, which is usually specified as inversely proportional to distances between inputs x and x' . We use a form known as the separable Matérn kernel (Stein, 1999) in our work, a conventional choice, parameterized by lengthscales θ and scale τ^2 . For details, see (Gramacy, 2020, Chapter 5). GPs provide a flexible, nonparametric regression tool. In addition to enjoying canonical status as surrogates for computer simulation experiments, they are utilized in geospatial statistics (Cressie and Wikle, 2011), time series (Roberts et al., 2013), and optimization (Jones et al., 1998).

GP surrogates are extremely effective. To illustrate, recall Figures 2 and 3 in Section 2.1, where limited samples of computer model evaluations ($n < 50$) are shown. For these toy examples, we “assumed” we had unlimited access to the simulator. In reality, we fit a GP surrogate to the model runs in the left panels. Therefore, “model runs” at posterior draws of u in the center panels are not in fact evaluations of the model, but predictions from a fitted GP surrogate. Even so, the Metropolis

sampler used those accurate (and fast) predictions to successfully recover the true model parameters u^* .

One downside to working with MVNs whose dimension grows with the dimension of the data they are trained on, n_M , is that building $n_M \times n_M$ matrices, and inverting (or otherwise decomposing) them, e.g., for Eq. (3) requires storage and computation that is quadratic and cubic in n_M , respectively. This limits n_M to a few thousand at most in a Bayesian MCMC setting, necessitating approximations for GPs that curb this prohibitive cost. With the 1d example in Figure 3, we have $n_M = 20 \times 30$, combining X and U , which is manageable. But for IBEX, the simulated sky maps like those in the middle and right panels of Figure 1 are in 2d (under the hood the output is in spherical coordinates x , y , and z) and results in $>16,000$ locations (or pixels) for each u -value. Combine that with $n = 66$ unique u -values used in runs available to us and our response vector will have greater than one million elements. Even if we used a smaller LHS space-filling design of size $n = 15$ over the model parameters, the response vector would still consist of over 200,000 points. In either case, an ordinary GP could not be fit and provide predictions in a reasonable amount of time, prompting the next topic.

2.3 Approximations

Most of our modeling effort in this paper involves circumventing the $O(n_M^3)$ computational bottleneck associated with GPs. The prevalence of methods addressing this issue has grown significantly in the past decade as increased access to computing resources leads to problems with larger and larger training datasets. These methods include, but are not limited to, fixed-rank kriging (Cressie and Johannesson, 2008), inducing points (Banerjee et al., 2008), compactly supported kernels (Kaufman et al., 2011), divide-and-conquer (Gramacy and Apley, 2015), and nearest neighbors (Datta et al., 2016; Wu et al., 2022). Most of these are general enough to be used in a variety of different fields and applications. However, there is a method tailor-made for our Bayesian inverse problem setting when the likelihood (for Y_F) is Gaussian.

Specifically in the context of (Gaussian) inverse problems, Higdon et al. (2008) faced computational bottlenecks much like the IBEX simulator: expensive simulations limiting runs and high-dimensional output in the form of images, shape description, time series, etc. Even with today’s computing resources, it would be prohibitive to fit a GP surrogate model on such large data. Higdon et al.’s key insight involved treating X^F (or gridded X) – i.e., the fixed reference set that a simulator realization is evaluated on for each candidate parameter u – as a feature of *output*, rather than conventionally as an input. As a result, model and field data share the same set of measurement locations, that is, $X = X^F$. In this way, X^M remains small, including only the unique combinations of unknown parameters u .

Then, rather than keep track of all of those outputs Y^M , indexed over X^F or X , dimensionality may be dramatically reduced via principal components analysis (PCA). Specifically, they proposed representing the vector output of a simulator model $m(\cdot, \cdot)$ as the sum of n_k basis functions k_1, k_2, \dots, k_{n_k} , each scaled by a corresponding weight $w_i(u)$: $m(u, X) \approx \sum_{i=1}^{n_k} k_i \cdot w_i(u)$, where $w_i(u) \sim \mathcal{N}(0, \Sigma_{w_i})$ and $n_k \ll n_X$. Weights $w_i(u)$ are each modeled as realizations of a zero-mean GP. By not directly modeling the high-dimensional response $m(\cdot, \cdot)$ and its associated dense grid X , requisite decompositions Σ_{w_i} avoid the cubic bottleneck in computation when scaling to large n

and can be completed in a reasonable amount of time.

While clever, this is one of those easy-to-say hard-to-do situations. The implementation is complex both mathematically, and in code. We are aware of only one library implementation, originally written in `MATLAB` and now deployed in `Python` (Gattiker et al., 2020). We found it difficult to appropriate that setup for our own use in a Poisson likelihood context. Additionally, restricting the simulated and field data to work on the same reference grid was not possible with IBEX’s orbital data locations (Figure 1).

Fortunately, GP approximation has come a long way in the last twenty or so years. Higdon et al. specifically lamented not having access to such technology, necessitating a more complex approach. It is no longer necessary to play the trick of moving a reference grid to the output space. A GP (approximation) may model Y^M via all inputs X^F and U via X^M , as we shall demonstrate next. The result is at once more modern, faster, and better compartmentalized for use in novel contexts, such as our own.

3 Vecchia Approximated GPs for IBEX Simulations

In 1988, Vecchia proposed an approximation for evaluating a multivariate normal density. The Vecchia approximation, say in the context of GP modeling with the likelihood for Y^M (i.e. $\mathcal{L}(Y^M)$), relies on the ability to write any joint probability as a cascade of univariate conditionals, which for GPs are Gaussian (3).

$$\begin{aligned} \mathcal{L}(Y^M) &= \prod_{i=1}^{n_M} \mathcal{L}(Y_i^M | Y_{g(i)}^M) \quad \text{where } g(1) = \emptyset \quad \text{and } g(i) = \{1, 2, \dots, i-1\} \\ &\approx \prod_{i=1}^{n_M} \mathcal{L}(Y_i^M | Y_{h(i)}^M) \quad \text{where } h(i) \subset \{1, 2, \dots, i-1\} \quad \text{and } |h(i)| \ll n_M \end{aligned} \quad (4)$$

Vecchia’s critical observation was that one could approximate this function by reducing the size of the conditioning set $g(i)$ to a much smaller size m , as specified by the user. This induces sparsity in the precision matrix (e.g. $\Sigma(X^M)^{-1}$) from Eq. 3, potentially dramatically speeding up the evaluation of the likelihood for large values of n_M . Katzfuss and Guinness (2021) recently made this approximation popular by working out its representation in matrix form and furnishing automatic $h(i)$ creation via nearest neighbors and publicly available code, allowing for broad use in a variety of different fields where GPs are employed, particularly spatial statistics and computer experiments (Guinness, 2018; Katzfuss et al., 2020; Katzfuss and Guinness, 2021; Zhang and Katzfuss, 2022; Sauer et al., 2023).

The Vecchia approximation takes an operation of order $O(n_M^3)$ down to $O(n_M m^3)$, motivating small values of m . Logically, as the size of $h(i)$ decreases, the evaluation of the likelihood speeds up, but the quality of the approximation is reduced. On the flip side, as one increases m , execution time grows, but the degree of accuracy improves. This continues until $n = m - 1$, when the likelihood is no longer an approximation. For the IBEX simulator data, we find a value of $m = 25$ to be more than sufficient.

Several implementations of the Vecchia approximation exist, but we employ one that has risen to the top in terms of predictive performance and computational thriftiness in the context of computer

experiments, that is, the Scaled Vecchia approximation introduced by Katzfuss et al. (2022). We refer you to their manuscript for a more in-depth explanation of their work, but the primary draw for using it as a surrogate for the IBEX simulator is the open source implementation and packaging that leverages modern sparse matrix libraries and parallel processing. Code that we directly rely on is readily accessible at <https://github.com/katzfuss-group/scaledVecchia>.

3.1 Surrogate Sky Maps

Figure 4 illustrates examples of conditioning sets created by the Scaled Vecchia approximation in the context of IBEX and its associated simulator. (We will circle back to the inverse problem and the data collected by the satellite in Section 4). Neighborhoods of size $m \in \{25, 50, 75, 100\}$ are generated for a particular simulator observation Y_i^M (denoted by a red star) from the IBEX computer model. It’s difficult to visualize in higher dimensions, so we break the input space down into separate 2d plots, one for grid space (latitude/longitude) and one for model parameter space (u). But to be clear, points of the same shape and color in both plots are elements of the same overall conditioning set. For each conditioning set $h_j(i)$, all points from sets where $m < m_j$ are also included in $h_j(i)$. That is, green circles from the neighborhood with $m = 25$ would also be part of the conditioning set with blue squares ($m = 50$). For reference, we’ve overlaid the points in grid space on a grayed-out simulated sky map corresponding with the observation of interest. Note that more points are concentrated near the reference point in latitude and longitude, whereas the neighborhood is more spread out over the unknown model parameters. Therefore, observations condition on information in close proximity in grid space, but potentially distant in u -space. Furthermore, as m grows, additional points in grid space are mostly farther away than those already included, but we don’t observe the same trend in u -space.

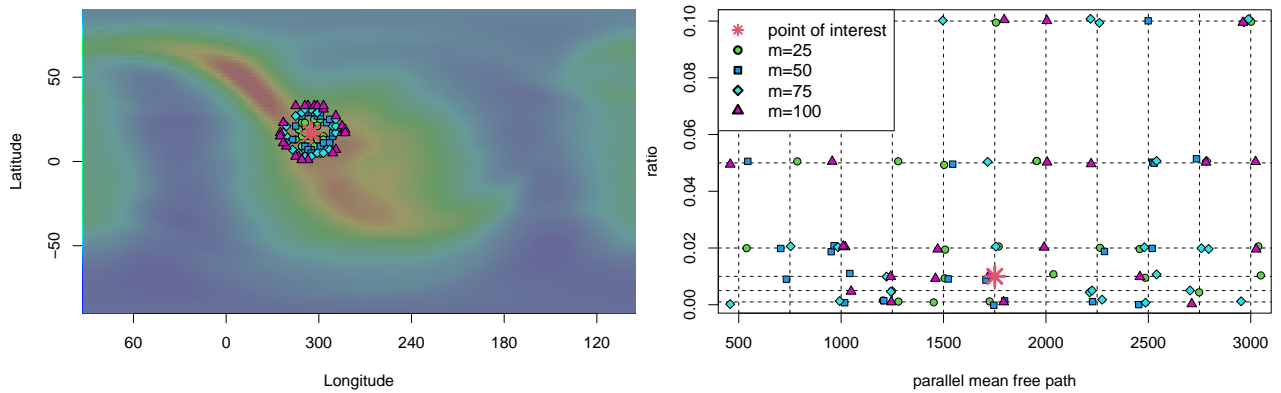


Figure 4: Conditioning sets $h(i)$ in a multivariate normal likelihood (Eq. 4) for a single observation Y_i^M using the Scaled Vecchia approximation. The left panel visualizes neighborhoods in grid space (i.e. X or X^F). Model parameter (u) space is displayed in the right panel with jitter added. Intersections of black, dashed lines indicate unique u combinations run on the simulator.

We begin evaluation of Scaled Vecchia’s performance on the IBEX simulator with a visual

assessment. Scientists at LANL have provided us with 66 unique model runs, each producing an image of 16,200 points, or pixels. Figure 5 shows four of the actual simulation outputs (corner panels displayed with thin, solid borders). A Scaled Vecchia surrogate is fit to all 66 simulated runs. Then, we predict the output for five unobserved combinations of the model parameters that fall in between the actual runs shown. These are depicted in the cross of Figure 5, those panels with thicker, dashed borders. To the naked eye, these predictive surfaces appear to have been generated by the computer model itself. Moving left to right, or top to bottom, the surfaces change gradually and as one would expect. Next we show empirically that our surrogate fit is accurate and outperforms competitors.

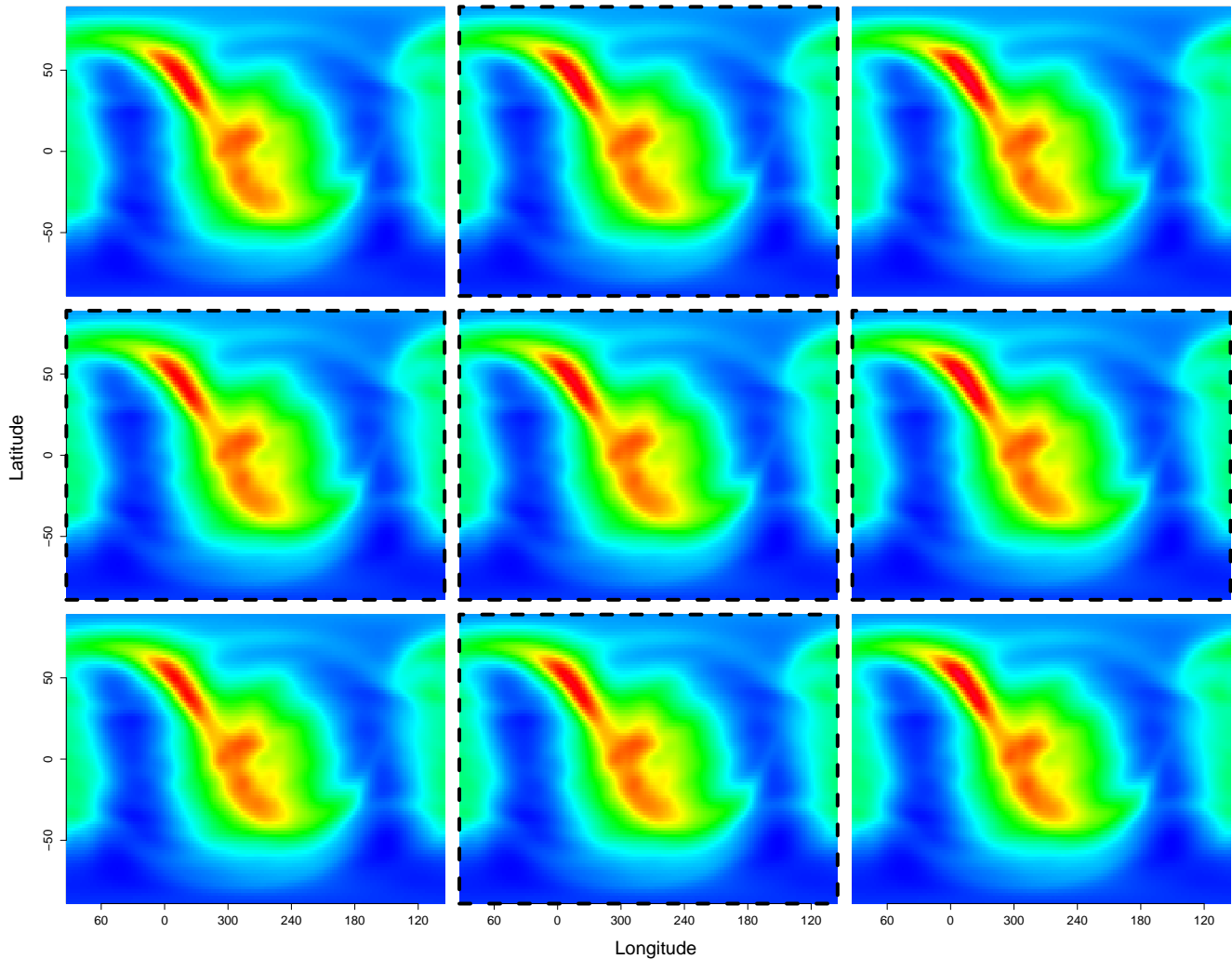


Figure 5: Actual and predicted outputs from the IBEX *sky map* computer model. Corner panels represent the response for four unique combinations of model inputs. Panels on the cross with bold, dashed borders are predictions at unobserved input combinations from a GP surrogate fit to $n = 66$ runs of the computer model. Model parameter settings for the predictive panels fall between the four actual simulator runs shown.

3.2 Empirical Comparison

To benchmark our surrogate, we conduct experiments to gauge predictive accuracy via root mean squared error (RMSE), uncertainty quantification via continuous ranked probability score (CRPS; Gneiting and Raftery, 2007), and computational efficiency via time. We carry out the same experiment for three competitors: R packages `laGP` (Gramacy and Sun, 2014) with defaults and `deepgp` (Booth, 2024) with 1000 MCMC iterations and `vecchia = TRUE`, and the current “status-quo” SEPIA (Gattiker et al., 2020) with $n_k = 3$, implemented in Python.

Figure 6 displays the accuracy results of a simple hold-one-out bakeoff, with time coming next. For each iteration of the experiment, we fit a Scaled Vecchia GP surrogate on 65 of the $n = 66$ model runs available. Then, we predict at the held out model parameter. For now, just pay attention to the boxplots on the left-hand side of each panel. We’ll come back to the others in a moment. It is obvious that the Scaled Vecchia approximation outperforms `laGP` and `deepgp` in both RMSE and CRPS. The local focus of `laGP` limits its ability to capture global trends, potentially hurting its performance. Large data and corresponding expensive matrix operations restrict the number of iterations `deepgp` can run and thus prevents the MCMC from converging to the target posterior. SEPIA performed similarly to our Scaled Vecchia approximation, illustrating why it has had such staying power over the past two decades. As a practitioner, it appears to be a toss-up between these two methods for which to use. But that’s not the entire story.

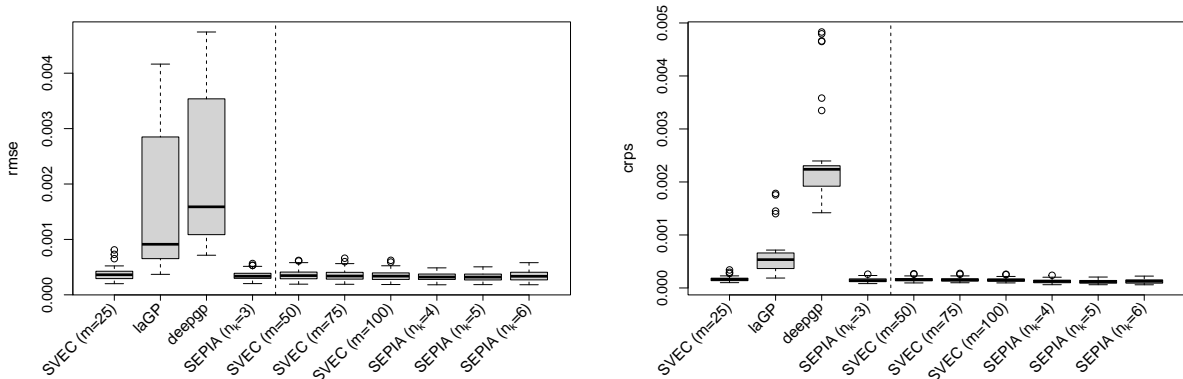


Figure 6: Metrics on the IBEX simulator experiment. Smaller is better for both RMSE and CRPS.

Figures 7-8 summarize compute times in a similar experiment but varying data size. Two factors exist that contribute to a computational bottleneck: the dimension of the simulator response (the main focus of our work), and the number of runs of the computer model available for training. To test the former, we vary the dimensionality of the response from 200 to 20,000, while keeping the number of runs constant. For the two methods that are best equipped for large dimensions (Scaled Vecchia and SEPIA), we attempt to stretch their capacity by cranking up the length of the response vector from 20-75K by steps of 5K. At each dimension size, we run five Monte Carlo iterations for each method and record the average elapsed time.

It is plainly visible from Figure 7 that Scaled Vecchia and SEPIA are both well-suited for

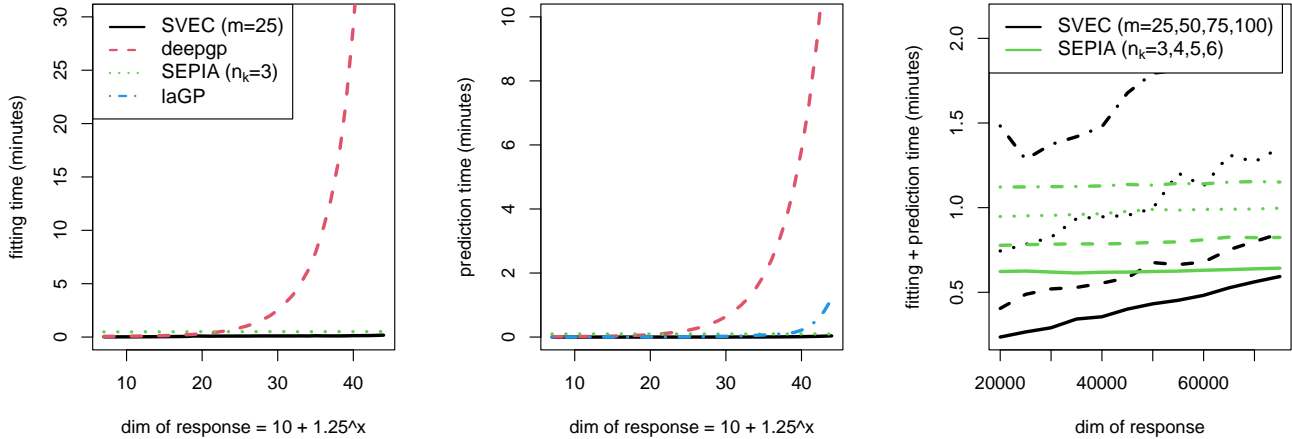


Figure 7: Timing metrics on the IBEX simulator experiment. A comparison of the fastest methods is shown in the right panel, with different line types indicating neighborhood size (m) and number of principal components (n_k) used for Scaled Vecchia and SEPIA, respectively.

increasing dimensionality in the response. Our **deepgp** competitor needs to decompose an $n_M \times n_M$ matrix at each MCMC iteration, which causes its cost to quickly grow as dimensionality expands, even aided by the Vecchia approximation. While **laGP** does better, it is unable to keep pace at a certain point, likely due to the need to fit a mounting number of local GPs separately for each testing location. Reducing the neighborhood size for **laGP** could help reduce computation, but would further degrade its accuracy. The comparison between Scaled Vecchia and SEPIA is more nuanced. In the right panel of Figure 7, we see that for a fixed value of m , Scaled Vecchia’s runtime increases linearly with expanded dimensionality, consistent with claims made by Katzfuss and Guinness (2021). For a fixed number of principal components, SEPIA’s execution time increases only slightly as dimension expands, showcasing its utility. However, for response dimension less than 75K, Scaled Vecchia with $m = 25$ still executes faster. And that may be the largest value of m we need. The boxplots on the right-hand side of each panel in Figure 6 show that increasing m or n_k doesn’t significantly improve performance. It must also be pointed out that the IBEX simulator surface is not particularly complex over the model parameters, allowing SEPIA to perform well with a low value of n_k . That may not be the case in other situations, requiring more principal components and by extension a heavier computational load.

Figure 8 displays timing results from changing the size of the training dataset (i.e, the number of simulator runs n). SEPIA was specifically built for computer experiments with high-dimensional output. While it clearly performs well in these situations, it’s also fairly inflexible to other contexts, such as a large number of simulation runs. Scaled Vecchia does not face this hurdle, as it treats both high-dimensional output and large-scale univariate datasets similarly, as a scalar response. Our experiment is set up similar to the previous one, but we keep the dimensionality of the response at 10K while sliding the number of simulator runs from 10 to 100. Again, all methods are run over five MC iterations for each value of n . For the higher performing methods, we push the campaign

size up further ($n = 2500$).

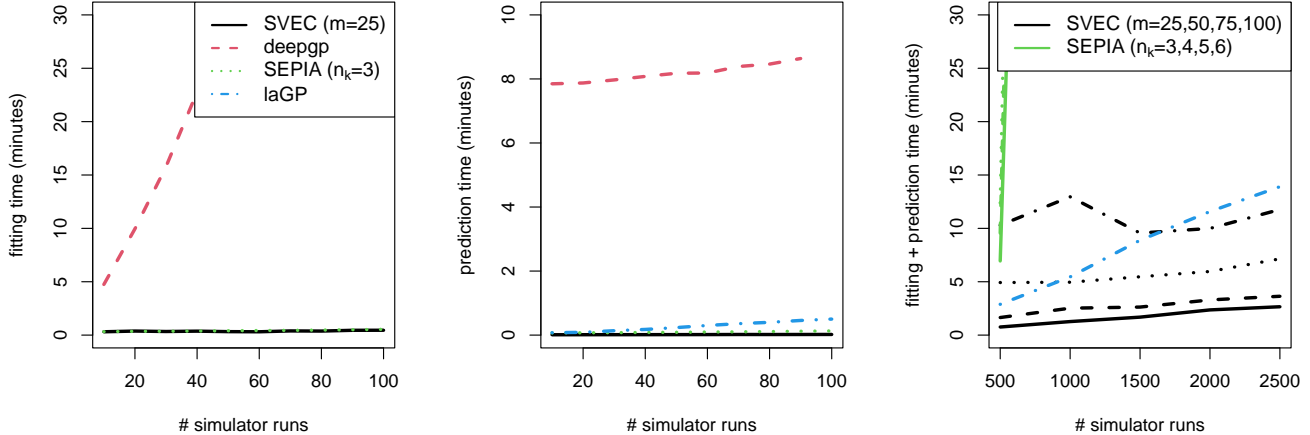


Figure 8: Timing metrics on the IBEX simulator experiment.

It’s no surprise that `deepgp` once again lags in run time. Even a modest sized set of runs takes well over an hour to fit and needs almost 10 minutes to make a single prediction. Most interesting is the behavior of SEPIA in the right panel of Figure 8. For $n > 500$, SEPIA takes hours to fit and make predictions. In this context, even `laGP` performs better. Our preferred method, Scaled Vecchia, shows consistency in scaling linearly with an increased campaign size and executes faster than each competitor when $m < 50$, and for all values of m when $n > 1500$.

4 IBEX Satellite Data

We now return to the IBEX inverse problem. We wish to determine the settings u of a computer model that produce a sky map most likely to have generated observed counts and, more specifically, quantify the uncertainty on our estimates of u . Before diving in, we dispense a few important details about IBEX observations and computer simulations. We then test our modeling apparatus on synthetic field observations (computer model at known u^* and with Poisson counts) to ensure good performance within the model class, and where we know the true calibration parameter. Finally, we report on our calibration of the actual IBEX satellite observations.

4.1 IBEX details

Each row of the satellite dataset contains Cartesian coordinates (x, y, z) for the direction the satellite was pointing, time the satellite was aimed at that location (in seconds), counts of ENAs observed at one of six different energy levels (ESA), and a background rate λ_b (ENAs/sec). Note that for the sake of brevity, we focus only on ENAs collected at energy level ESA 4. More important to consider is that ENAs are known to come from sources other than the heliosphere. Space scientists quantify

this noise for each location (X^F) viewed by the satellite and add it as a background rate (λ_b) that must be accounted for in the data. For example, the left panel of Figure 1 displays ENA rates *after* λ_b has been subtracted out. Although this rate is an estimate rather than an exact value, we follow the lead of other researchers (Osthus et al., 2023) and treat it as constant in our work. For the purpose of solving the inverse problem, we address this through an update to the mean expression in the Poisson likelihood in Eq. 2 such that $\lambda(X^F) = m(u, X^F) - \lambda_b(X^F)$.

We have referred to the IBEX simulator throughout this paper without going into much detail. While we leave a more in-depth physical interpretation and analysis of parameters to more appropriate venues (Zirnstein et al., 2021b, 2025; Swaczyna et al., 2020; Huang et al., 2025), some basic context is provided here. We focus on two particular models available (among many): one for the GDF and one for the ribbon. In the ribbon model, the parameter *parallel mean free path* is the distance a hydrogen ion travels beyond the heliopause, or edge of the heliosphere, before interacting with another particle, receiving an electron and becoming an ENA, and “turning back.” The *ratio* parameter is the fraction of perpendicular mean free path, another measure of distance, and *parallel mean free path*. These are our u values. The response from the GDF model is static and is merely added to the output of the ribbon simulator. This is not the case for GDF simulators in general, but the GDF model we have access to does not vary with any parameters of interest.

Scientists know that the makeup of the heliosphere evolves over time, largely due to variations in the solar wind that accompany the approximately 11 year solar cycle. Physicists build these changes into their simulators either through additional parameters, restricting the application of their models to a specific timeframe, or simply averaging over the solar cycle. The GDF model we utilize was developed to correspond to the years 2009-2011, while the ribbon model averages the composition of the heliosphere over the entire solar cycle. We factor in these heliospheric variations by only comparing satellite data from the years 2009-2011 to simulator runs.

4.2 Synthetic testbed for inverse problem validation

Using the corpus of $n = 66$ computer model runs, varying a design of *parallel mean free path* and *ratio* u -values, described in Section 3, we select a value u^* and set the corresponding output ($\lambda^* = m(u^*, X^M)$) as the “true” underlying mean ENA rate (upper right panel of Figure 9). Next, we gather measurement locations X^F , exposure times e , and background rates λ_b from a single year that the IBEX satellite has been in operation, ignoring the observed counts of ENAs in this fabricated example. For each latitude/longitude pair (i.e. a row in X^F), we draw synthetic satellite (or field) data from a Poisson, $Y_i^F \sim \text{Pois}(\lambda_i^* + \lambda_{b_i}, e_i)$, where λ_i^* is determined by the computer model $m(\cdot, \cdot)$. The top left panel of Figure 9 shows the result, which we will regard as data we “observed.” Note that observations are not on a fine grid, but instead match the recorded coordinates for ENAs captured by the IBEX satellite in its orbit. This accounts for the unique spread of points and the strings of missing data, which correspond to certain orbits.

We run Algorithm 1, treating this synthetic data as (X^F, Y^F) and fitting a Scaled Vecchia GP surrogate on the provided computer model output (omitting responses for u^*) as (X^M, λ^M) . It should be noted that we employ an empirical Bayes approach (Berger, 1985; Kennedy and O’Hagan, 2001), pre-estimating the GP hyperparameter θ and only fitting the surrogate on simulator output (Liu et al., 2009). We execute 10,000 MCMC iterations, throwing away 1,000 as burnin and thinning

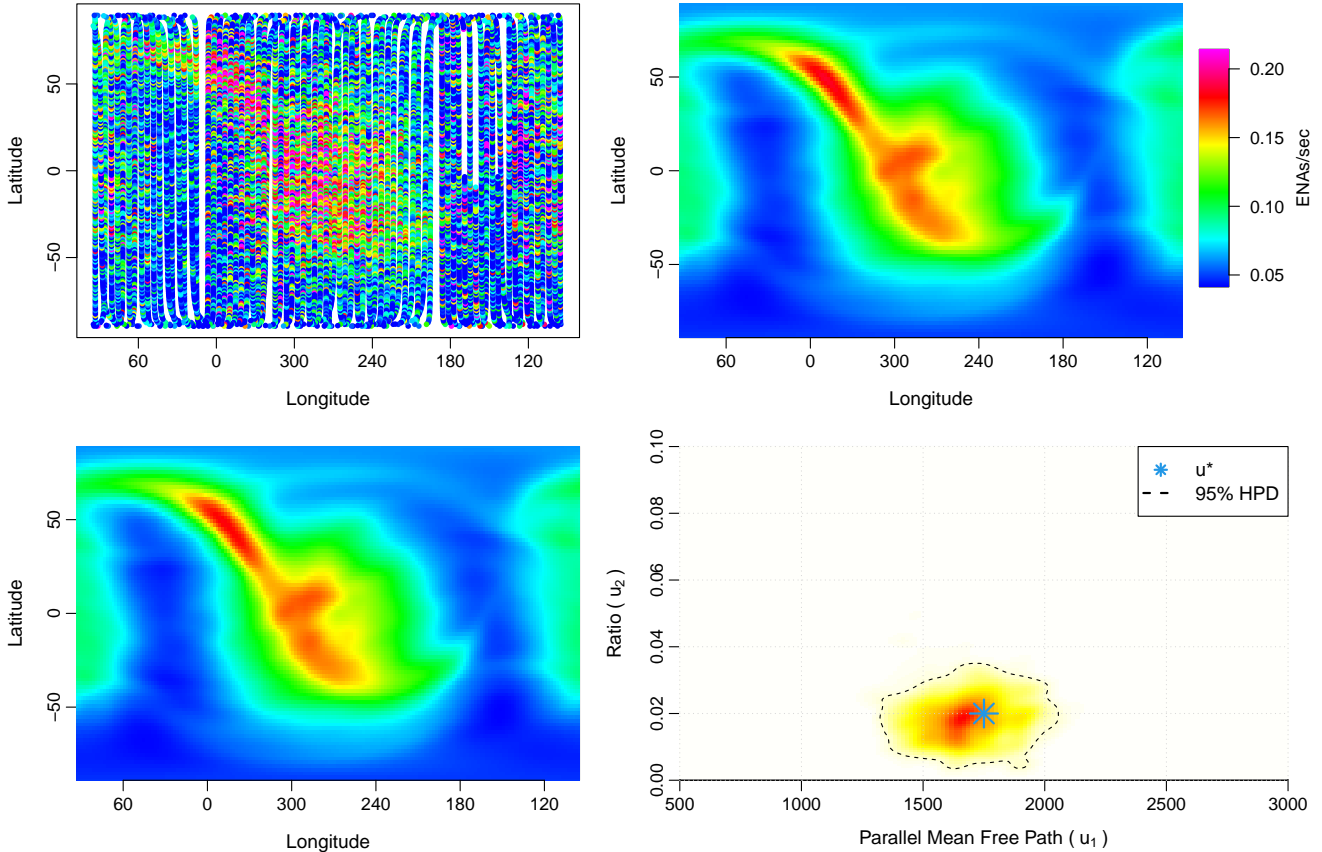


Figure 9: Estimate of ENA rate (counts/seconds) based on synthetic Poisson draws from a “true” computer model setting and varying exposure times (top left). IBEX simulator output of ENA rate at *parallel mean free path* = 1750 and *ratio* = 0.02 (top right). Predicted output via a fitted Scaled Vecchia surrogate at estimated calibration parameters (bottom left). Posterior samples of model parameter u as a kernel density (bottom right).

by 10. Figure 9 displays the remaining posterior samples of u (bottom right) as a kernel density along with a 95% highest posterior density (HPD) interval. The posterior mean of $u \mid Y^F$ lies near u^* , demonstrating that our framework is able to concentrate mass around the “true” model parameter. As a sanity check, we take the estimated posterior mean and plug it in to our fitted Scaled Vecchia GP surrogate of the IBEX simulator. The predicted output is shown in the bottom left panel of Figure 9. There are some nearly imperceptible differences between the estimated sky map and the true λ^* (i.e, the shape and intensity of the ribbon vary slightly between the two). However, from a purely visual standpoint, it appears that each map could have reasonably generated the data we “observe” in the top left panel.

To further validate our methodology, we apply this method to each unique model parameter available. We have access to simulator runs representing all combinations for 11 unique values of parallel mean free path and 6 unique values of ratio ($n = 66$). The spread of parameter values is determined by space scientists to include all values considered reasonable: parallel mean free path

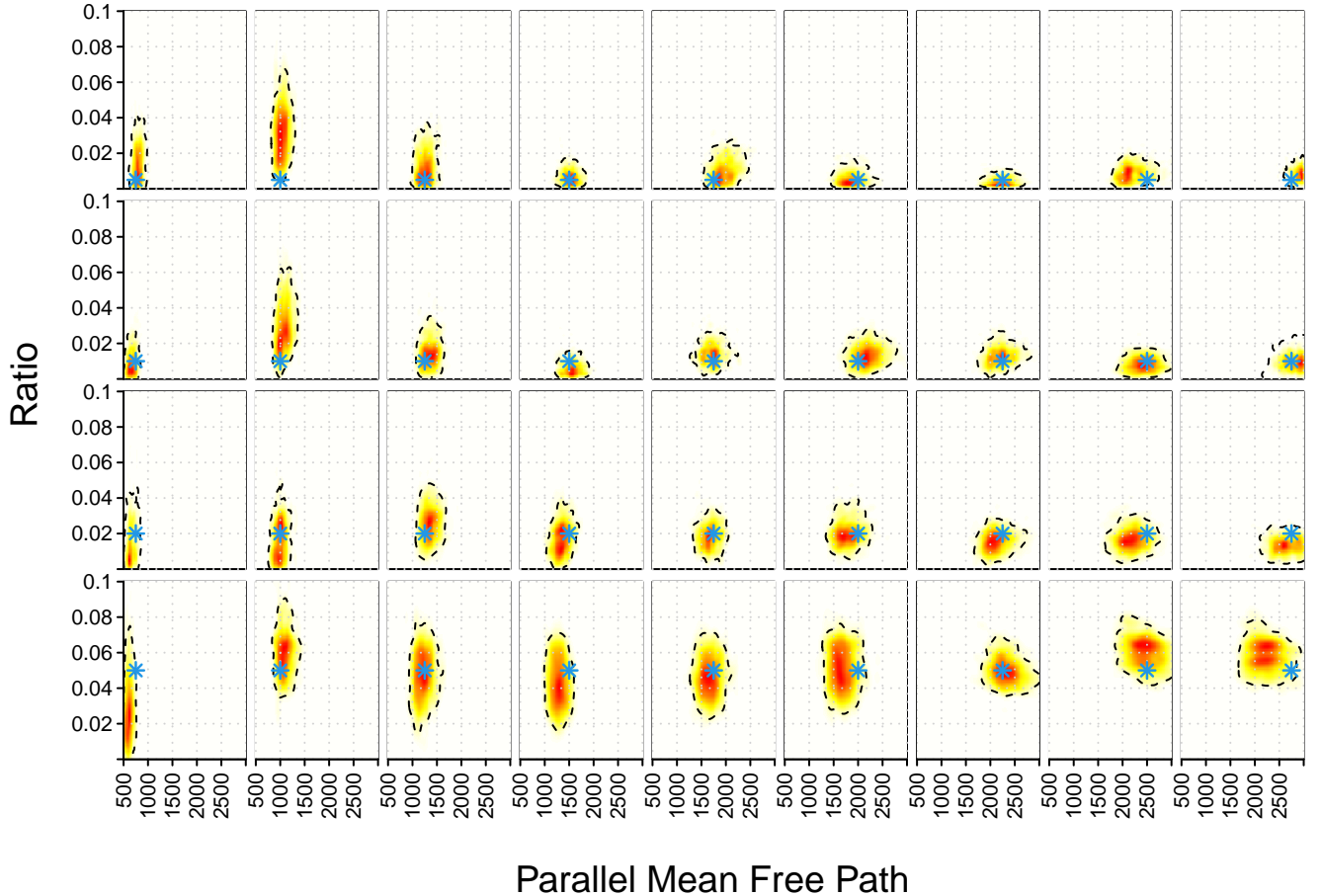


Figure 10: Posterior distributions $u \mid Y^F$ and 95% HPD intervals from runs of our Poisson Bayesian inverse problem framework on 36 different synthetic datasets. Blue stars indicate the value u^* from which the data was simulated.

ranges from 500-3000 astronomical units (AU); ratio values are unitless, and span from 0.001 to 0.1. Due to the inability for the model to furnish posterior samples beyond the boundary parameters, we do not test those combinations for which at least one parameter is on its edge (i.e, when parallel mean free path $\in \{500, 3000\}$ and/or ratio $\in \{0.001, 0.1\}$). Removing these edge cases results in 36 remaining test runs. For each combination, we follow the same procedure as above: select one model parameter and set as u^* , create simulated observed satellite data, fit a Scaled Vecchia surrogate on training data excluding u^* , and run Algorithm 1 to sample from the posterior $u \mid Y^F$. Results are shown in Figure 10.

Each panel shows posterior samples of $u \mid Y^F$ for a unique u^* as a kernel density. We have indicated each u^* that generated synthetic Y^F as a blue star. Our 95% HPD intervals encompass the truth in 34 of the 36 of the iterations, near the nominal coverage rate we'd expect. Therefore, we can confidently assert that our proposed framework is able to recover the “true” parameter values from *synthetic* satellite data. Next, we apply this to real data, with the goal of helping scientists

better understand the behavior of the heliosphere by estimating these parameters for actual ENA counts collected by the IBEX satellite.

4.3 Real IBEX ENAs

Our experimental setup will be similar to that in Section 4.2, only substituting in real data for simulated data. Space scientists at LANL have provided us with satellite data from IBEX for the years 2009-2011, aligning with the implementation of the computer model. The number of records in each sky map varies across the three years from $\sim 7\text{-}9\text{K}$ observations, giving us over 23K rows of field data (X^F, Y^F) for use in our analysis. We execute Algorithm 1 by fitting a Scaled Vecchia GP surrogate to *all* 66 computer model runs and sample from the posterior $u \mid Y^F$ via MCMC. One difference from Section 4.2 is that field data (X^F, Y^F) are not exclusively from one map (Figure 11). Instead, (X^F, Y^F) is formed by stacking the counts, exposure times, background rates, and Cartesian coordinates x, y, z from years 2009-2011.

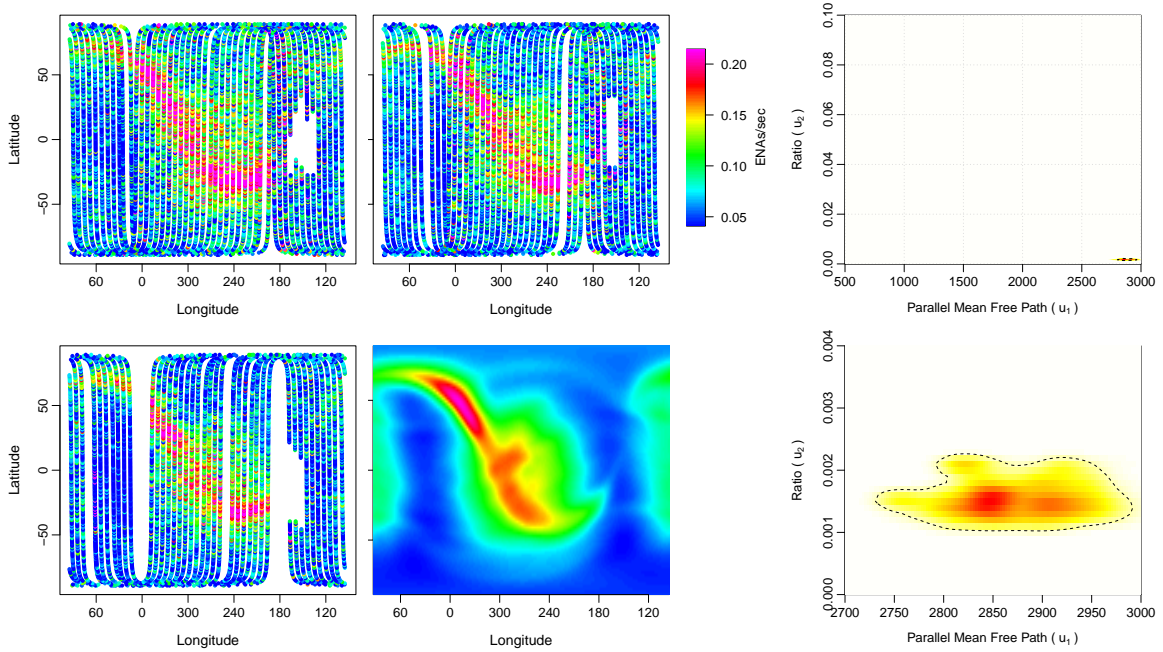


Figure 11: Observed IBEX satellite data for years 2009-2011 (top left, top middle, bottom left). Predicted output via a fitted Scaled Vecchia surrogate at estimated model parameters (bottom middle). Two views for the posterior distribution of sampled model parameters u (top right, bottom right).

Figure 11 makes it evident that the predicted GP surrogate output at the posterior mean of $u \mid Y^F$ marks a clear difference from the trends observed in real data. In particular, the intensity of the ribbon in the surrogate prediction near latitude -30° and longitude 240° appears to be much lower than what is observed in the satellite data for each year. There's also a gap (in this instance overestimating the ENA rate) between surrogate and reality between longitudes 60° and 120° and latitudes $\pm 50^\circ$. Another indication of this clash is visible in the right panels of Figure 11. Note that

these both display the same posterior distribution, but differ in their axis limits. Posterior mass is concentrated in the extreme corner of the model parameter space. Our priors attempt to push sampling away from the boundaries, but the likelihood dominates the posterior. We take this as an indication that the computer model is lacking in its attempt to represent reality, and the Metropolis sampler seeks to go beyond the range of model parameters present in the training data.

The boundary-pushing estimate for u and the gap, which is plainly visual between surrogate predictions and collected data, are somewhat unsatisfying. We address in more detail the potential discrepancy between simulator and reality in Section 5. But we wish to offer some validation that our method performs well for the real data, *given* our provided computer model implementation and the available runs. To do so, we ran a final experiment using cross validation and calculation of CRPS at testing locations. We split the satellite data from 2009-2011 into ten equally-sized folds. For each fold f , we ran our Poisson Bayesian inverse problem framework as before, but only use the other nine folds as field data, and store the resulting model parameter estimate, \hat{u}_f . Note that for each fold, all computer model output is still used to train the surrogate. We then predict the underlying ENA rate λ at the held out field data locations in three separate manners: 1) over a fine grid of parallel mean free path, with ratio fixed at the posterior mean of u_f ; 2) over a fine grid of ratio, with parallel mean free path fixed at the posterior mean; and 3) over a fine grid of both parallel mean free path and ratio. We calculate CRPS for all predictions.

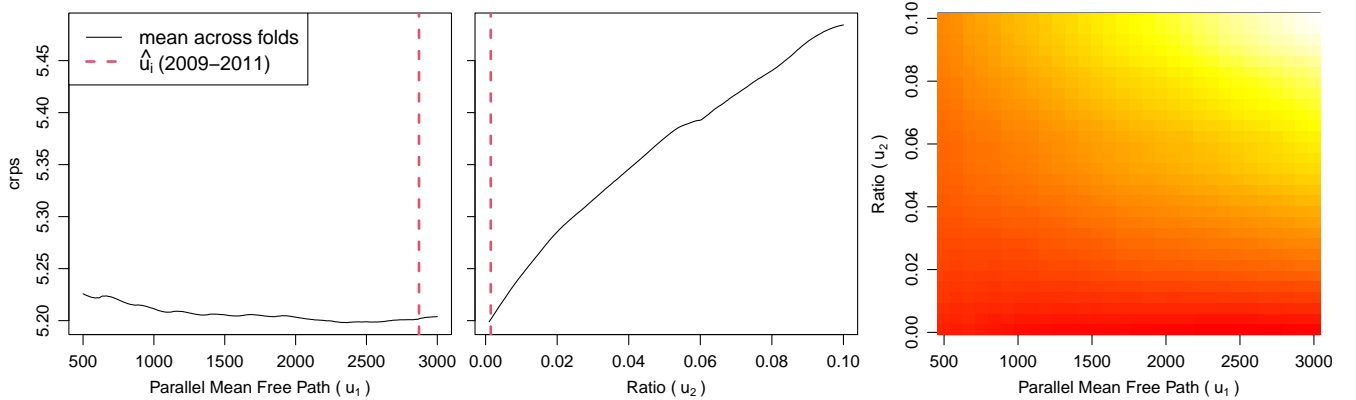


Figure 12: Metrics from a cross-validation experiment for IBEX satellite data. Averaged CRPS across folds on fine grids of parallel mean free path and ratio (left and middle) and a lattice over both (right). In the right panel, low values are in red and high values are in yellow. Lower CRPS indicates better performance.

The outcome of this experiment is summarized in Figure 12. The left and middle panels display CRPS for surrogate predictions using 200 equally-spaced values of parallel mean free path and ratio, respectively, at held-out satellite data locations. CRPS is averaged over the ten folds. For reference, we include a red dashed line to mark our estimate of the model parameter u_i when using all the IBEX data from 2009-2011. It's clear that the setting of the ratio parameter largely determines how well the surrogate predictions fit the real data. CRPS changes significantly across the entire

range of ratio, but only shifts slightly for parallel mean free path. Furthermore, looking back at Figure 11, note that the posterior (bottom right panel) is spread across a broad set of values for parallel mean free path ($\sim 2700-3000$). That ridge or plateau-like behavior lines up with our results here, as that spectrum of parallel mean free path corresponds to ones that lead to low values of CRPS (left panel) in this cross-validation experiment. The right panel of Figure 12 shows CRPS, averaged across ten folds, for surrogate predictions on a 30×30 grid over both model parameters. There appears to be some interaction between the two parameters. Adjusting parallel mean free path when ratio = 0.1 greatly affects CRPS, going from red-orange to yellow-white. However, when ratio = 0.001, varying parallel mean free path stays fairly constant. The importance of parallel mean free path therefore lessens as ratio decreases in value, consistent with the posterior in Figure 11.

The take-home message from Figure 12 is that the mean of posterior samples $u \mid Y^F$, when using the complete satellite dataset and the *available* computer model output, performs well in terms of CRPS. That is, our estimate of u resides in the region with settings of parallel mean free path and ratio that result in the lowest values of CRPS across the supplied parameter bounds. Therefore, given the constraints (i.e, bias from reality) of a specific computer model and the u -values provided in a campaign of simulator runs, we can be confident that our Bayesian framework concentrates posterior mass at the best possible value of the model parameter u .

5 Discussion

We have introduced an effective tool for solving inverse problems using Bayesian methods where 1) the simulator representing the physical model or process is expensive, limiting the number of runs available for analysis and demanding a GP surrogate, but 2) the computer model output is extremely high-dimensional, requiring novel methods to induce sparsity and approximate the GP, and 3) data from a field experiment are Poisson counts, bucking the current Bayesian inverse problem literature that focuses on normally distributed field observations. Our proposed Poisson Bayesian inverse problem framework fills this gap by introducing a modular approach that satisfies all three requirements. We have shown that our framework is able to recover the model parameter u^* at the nominal 95% rate when provided with synthetic data where the “truth” is known and all modeling assumptions have been satisfied. We applied this methodology to a subset of data collected by the IBEX satellite from 2009-2011 and corresponding simulated heliospheric sky maps from a sophisticated computer model.

The IBEX satellite has collected counts of ENAs for over 15 years. Our work focused on data collected in a three-year period for which the computer model we relied on was aligned. Figure 13 shows resulting estimated posterior distributions for model parameter u when field data is split by year (2012-2021). Behavior is similar to what we observed in Figure 11, but even more extreme, as the Metropolis sampler pushes up against the boundary of the current range of u . We certainly do not claim these posteriors to be the true distribution of parallel mean free path and ratio. Instead, we suggest our work be extended to account for un-modeled discrepancy and paired with computer simulations that integrate other phenomena not represented in this paper and/or match years outside of 2009-2011.

Figure 14 displays the discrepancy between what the Scaled Vecchia surrogate of our computer

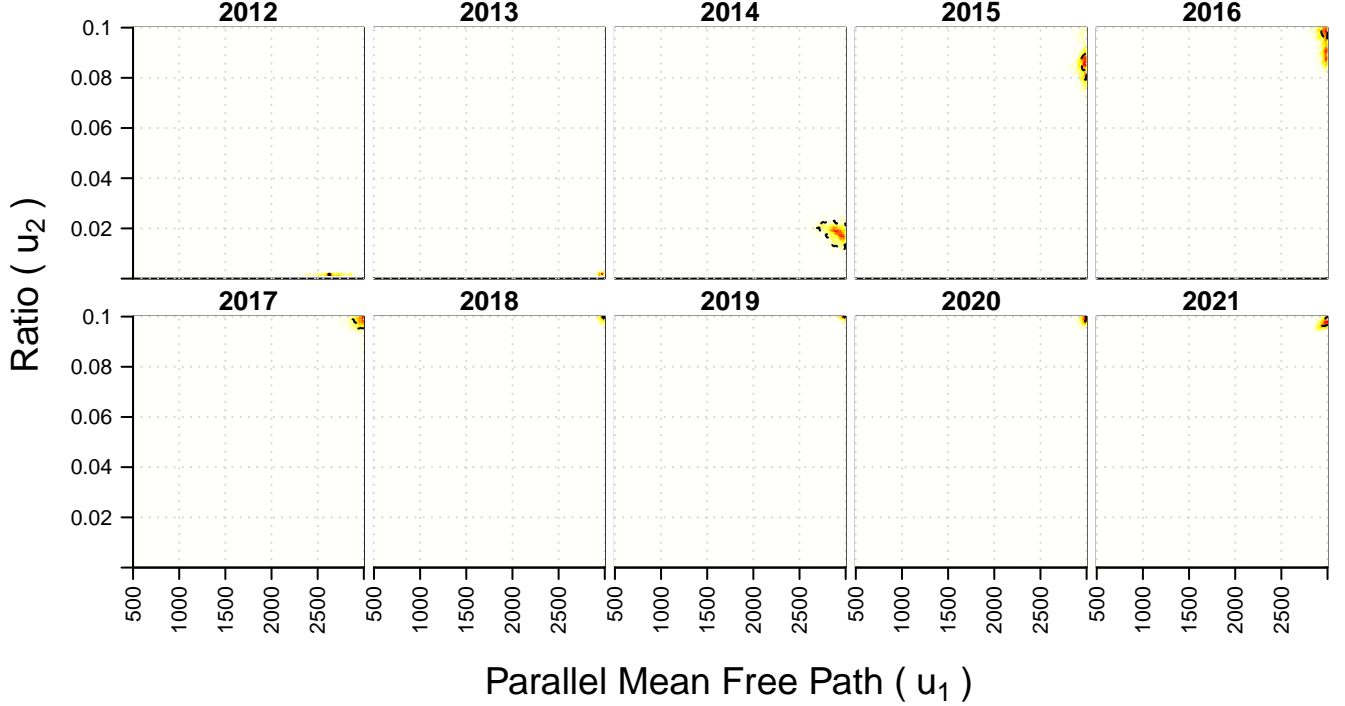


Figure 13: Posterior distributions $u \mid Y^F$ and 95% HPD intervals for 10 separate runs of our Poisson Bayesian inverse problem framework. Field data (X^F, Y^F) for each run come from a single year between 2012-2021.

model outputs at the posterior mean estimated by our framework for the model parameter u and data collected from the IBEX satellite in the years 2009-2011. It's clear that the computer model does not sufficiently account for the behavior observed in the satellite data. But this is not terribly surprising. Simulators are inherently biased, simply from not being able to completely reconstruct the real process. Kennedy and O'Hagan (2001) address this limitation by introducing a discrepancy term in their canonical computer model calibration framework, a practice followed by many other practitioners (Higdon et al., 2004, 2008; Liu et al., 2009).

The KOH approach uses a GP for modeling of complex disparities between simulator and reality. Due to our field response being counts, further methodology needs to be developed to apply the same GP discrepancy methods to IBEX, a point we leave to future work. However, we test the addition of a simple, multiplicative discrepancy term δ to our original model, modifying Eq. (2) as follows:

$$\begin{aligned}
 Y^F &\sim \text{Pois}(\lambda(X^F), e(X^F)) & \lambda(X) &= m(u, X) \\
 \lambda(X^F) &= \lambda(X) * \delta & \log(\delta) &\sim \mathcal{N}(0, 1) \\
 u &\sim \pi(u) & \text{e.g., } u &\sim \text{Unif}[0, 1]^p.
 \end{aligned} \tag{5}$$

The bottom right panel of Figure 14 shows posterior samples of δ . Mass is concentrated just below 1, indicating nearly zero effect from the multiplicative discrepancy. Examining the disparities

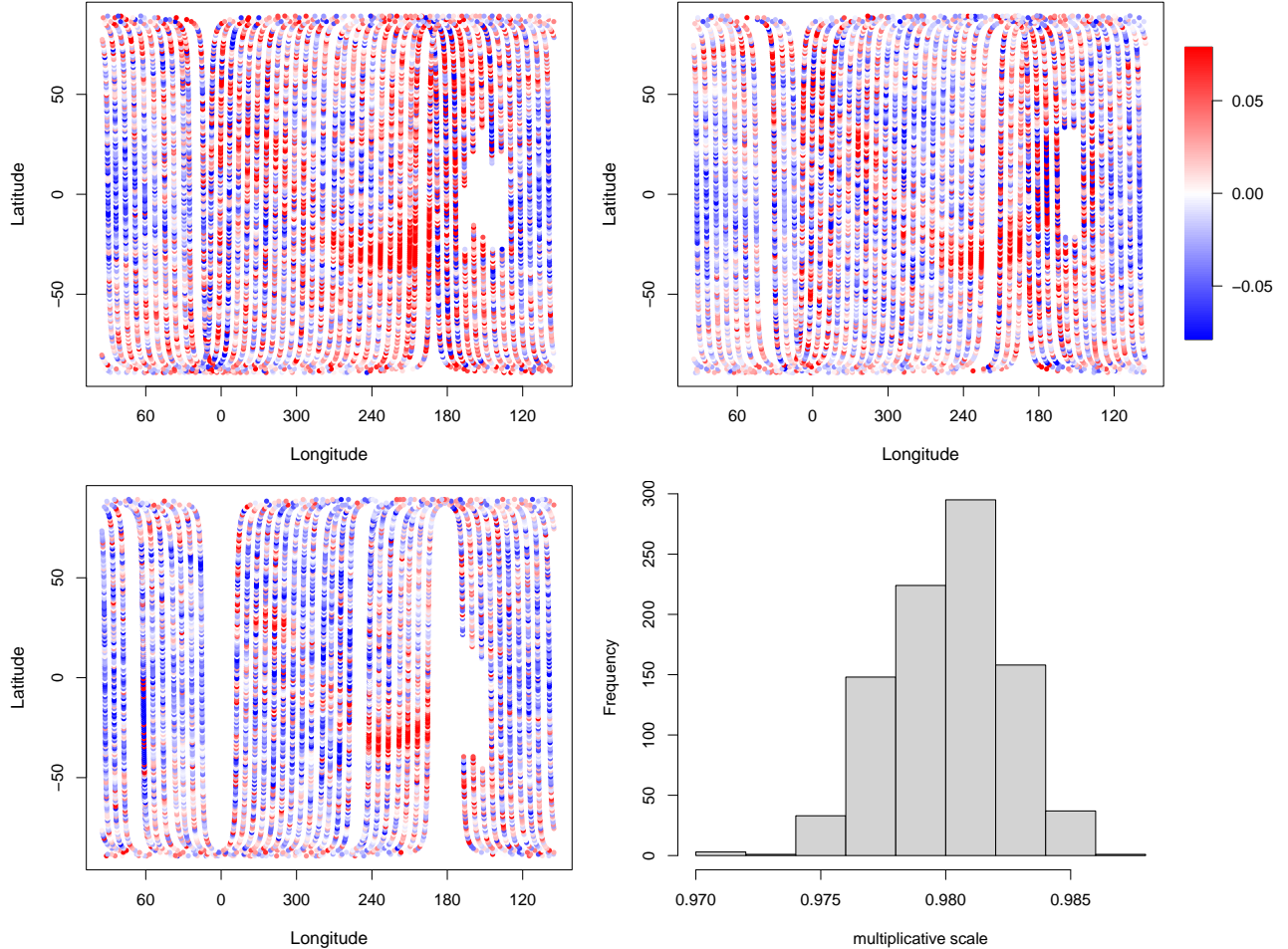


Figure 14: Discrepancy (observed - estimated) between observed satellite data and the simulator output at estimated model parameters in 2009 (top left), 2010 (top right), and 2011 (bottom left). Posterior samples of a multiplicative scale discrepancy (bottom right).

closer, it appears that spatial dependence exists in whether the simulator overestimates or underestimates the mean surface. For instance, the area of the sky map corresponding to the ribbon shows some underestimation. By contrast, areas outside of the ribbon are overestimated. A constant multiplicative scale discrepancy is clearly insufficient. We believe that δ is estimated around 1.0 because of these competing interests between different regimes in the sky map. More advancements are needed to properly model this disparity. A fully Bayesian framework could be developed to provide full uncertainty quantification, perhaps with the use of a deep Gaussian process to handle the inherent nonstationarity in the discrepancy.

We recognize that this is not a definitive calibration for IBEX data and some oversimplifications were made to fit our narrative and present a more generalizable method. Future work could account for details such as the Compton-Getting effect (Compton and Getting, 1935), spatial blurring resulting from the IBEX-Hi point spread function (Funsten et al., 2009), and varying parameters within a GDF computer simulation. We see the results in this paper as a first step in iteration

with the theoretical physicists on our team toward the development of a higher fidelity model which more faithfully reproduces dynamics observed in the field.

Data Availability

The authors confirm that data and code supporting the conclusions of this research, along with reproductions of included figures and examples, can be found at <https://github.com/lanl/ibex-bayesian-inverse>.

Acknowledgments

RBG and SDB are grateful for funding from NSF CMMI 2152679. SDB, DO and LJB were funded by Laboratory Directed Research and Development (LDRD) Project 20220107DR. This work has been approved for public release under LA-UR-25-30539.

References

- Banerjee, S., Gelfand, A. E., Finley, A. O., and Sang, H. (2008). “Gaussian predictive process models for large spatial data sets.” *Journal of the Royal Statistical Society Series B: Statistical Methodology*, 70, 4, 825–848.
- Berger, J. O. (1985). *Statistical decision theory and Bayesian analysis*. Springer.
- Booth, A. S. (2024). `deepgp`: *Bayesian Deep Gaussian Processes using MCMC*. R package version 1.1.3.
- Compton, A. H. and Getting, I. A. (1935). “An apparent effect of galactic rotation on the intensity of cosmic rays.” *Physical Review*, 47, 11, 817.
- Cressie, N. and Johannesson, G. (2008). “Fixed rank kriging for very large spatial data sets.” *Journal of the Royal Statistical Society Series B: Statistical Methodology*, 70, 1, 209–226.
- Cressie, N. and Wikle, C. K. (2011). *Statistics for spatio-temporal data*. John Wiley & Sons.
- Czado, C., Gneiting, T., and Held, L. (2009). “Predictive model assessment for count data.” *Biometrics*, 65, 4, 1254–1261.
- Datta, A., Banerjee, S., Finley, A. O., and Gelfand, A. E. (2016). “Hierarchical nearest-neighbor Gaussian process models for large geostatistical datasets.” *Journal of the American Statistical Association*, 111, 514, 800–812.
- Dawid, A. P. (1984). “Present position and potential developments: Some personal views statistical theory the prequential approach.” *Journal of the Royal Statistical Society: Series A (General)*, 147, 2, 278–290.
- Diebold, F. X., Gunther, T. A., and Tay, A. (1997). “Evaluating density forecasts.”

- Funsten, H., Allegrini, F., Bochsler, P., Dunn, G., Ellis, S., Everett, D., Fagan, M., Fuselier, S., Granoff, M., Gruntman, M., Guthrie, A., Hanley, J., Harper, R., Heirtzler, D., Janzen, P., Kihara, K., King, B., Kucharek, H., Manzo, M., Maple, M., Mashburn, K., McComas, D., Moebius, E., Nolin, J., Piazza, D., Pope, S., Reisenfeld, D., Rodriguez, B., Roelof, E., Saul, L., Turco, S., Valek, P., Weidner, S., Wurz, P., and Zaffke, S. (2009). “The interstellar boundary explorer high energy (IBEX-Hi) neutral atom imager.” *Space Science Reviews*, 146, 1, 75–103.
- Fuselier, S., Allegrini, F., Funsten, H., Ghielmetti, A., Heirtzler, D., Kucharek, H., Lennartsson, O., McComas, D., Möbius, E., Moore, T., Petrinec, S., Saul, L., Scheer, J., Schwadron, N., and Wurz, P. (2009). “Width and variation of the ENA flux ribbon observed by the Interstellar Boundary Explorer.” *Science*, 326, 5955, 962–964.
- Gattiker, J., Klein, N., Hutchings, G., and Lawrence, E. (2020). “lanl/SEPIA: v1. 1.” *Zenodo [code]*, 10.
- Gneiting, T., Balabdaoui, F., and Raftery, A. E. (2007). “Probabilistic forecasts, calibration and sharpness.” *Journal of the Royal Statistical Society Series B: Statistical Methodology*, 69, 2, 243–268.
- Gneiting, T. and Katzfuss, M. (2014). “Probabilistic forecasting.” *Annual Review of Statistics and Its Application*, 1, 1, 125–151.
- Gneiting, T. and Raftery, A. E. (2007). “Strictly proper scoring rules, prediction, and estimation.” *Journal of the American statistical Association*, 102, 477, 359–378.
- Gramacy, R. B. (2020). *Surrogates: Gaussian Process Modeling, Design and Optimization for the Applied Sciences*. Boca Raton, Florida: Chapman Hall/CRC. <http://bobby.gramacy.com/surrogates/>.
- Gramacy, R. B. and Apley, D. W. (2015). “Local Gaussian process approximation for large computer experiments.” *Journal of Computational and Graphical Statistics*, 24, 2, 561–578.
- Gramacy, R. B., Bingham, D., Holloway, J. P., Grosskopf, M. J., Kuranz, C. C., Rutter, E., Trantham, M., and Drake, R. P. (2015). “Calibrating a large computer experiment simulating radiative shock hydrodynamics.” *The Annals of Applied Statistics*, 9, 3, 1141–1168.
- Gramacy, R. B. and Sun, F. (2014). “laGP: Local approximate Gaussian process regression.” *R package version*, 1, 1–4.
- Grosskopf, M., Bingham, D., Adams, M. L., Hawkins, D., and Perez-Nunez, D. (2020). “Generalized Computer Model Calibration for Radiation Transport Simulation.” *Technometrics*, 63, 1, 27–39.
- Guinness, J. (2018). “Permutation and grouping methods for sharpening Gaussian process approximations.” *Technometrics*, 60, 4, 415–429.
- Higdon, D., Gattiker, J., Williams, B., and Rightley, M. (2008). “Computer model calibration using high-dimensional output.” *Journal of the American Statistical Association*, 103, 482, 570–583.

- Higdon, D., Kennedy, M., Cavendish, J. C., Cafo, J. A., and Ryne, R. D. (2004). “Combining Field Data and Computer Simulations for Calibration and Prediction.” *SIAM Journal on Scientific Computing*, 26, 2, 448–466.
- Huang, Y., Guo, F., Zirnstein, E. J., Noh, S. J., Li, H., Reisenfeld, D. B., and Heerikhuisen, J. (2025). “A Numerical Model for the Dynamics of Pickup Ions Outside the Heliopause and IBEX “Ribbon” Observation.” *The Astrophysical Journal*, 987, 2, 192.
- Jones, D. R., Schonlau, M., and Welch, W. J. (1998). “Efficient global optimization of expensive black-box functions.” *Journal of Global optimization*, 13, 455–492.
- Kaipio, J. P. and Fox, C. (2011). “The Bayesian framework for inverse problems in heat transfer.” *Heat Transfer Engineering*, 32, 9, 718–753.
- Katzfuss, M. and Guinness, J. (2021). “A general framework for Vecchia approximations of Gaussian processes.” *Statistical Science*, 36, 1, 124–141.
- Katzfuss, M., Guinness, J., Gong, W., and Zilber, D. (2020). “Vecchia approximations of Gaussian-process predictions.” *Journal of Agricultural, Biological and Environmental Statistics*, 25, 383–414.
- Katzfuss, M., Guinness, J., and Lawrence, E. (2022). “Scaled Vecchia Approximation for Fast Computer-Model Emulation.” *SIAM/ASA Journal on Uncertainty Quantification*, 10, 2.
- Kaufman, C. G., Bingham, D., Habib, S., Heitmann, K., and Frieman, J. A. (2011). “Efficient emulators of computer experiments using compactly supported correlation functions, with an application to cosmology.” *The Annals of Applied Statistics*, 5, 4, 2470–2492.
- Kennedy, M. and O’Hagan, A. (2001). “Bayesian calibration of computer models.” *Journal of the Royal Statistical Society: Series B (Statistical Methodology)*, 63, 3, 425–464.
- Knapik, B. T., Van Der Vaart, A. W., and van Zanten, J. H. (2011). “Bayesian inverse problems with Gaussian priors.” *The Annals of Statistics*, 2626–2657.
- Liu, F., Bayarri, M. J., and Berger, J. O. (2009). “Modularization in Bayesian analysis, with emphasis on analysis of computer models.” *Bayesian Analysis*, 4, 119–150.
- Matheron, G. (1963). “Principles of geostatistics.” *Economic geology*, 58, 8, 1246–1266.
- McComas, D., Allegrini, F., Bochsler, P., Bzowski, M., Collier, M., Fahr, H., Fichtner, H., Frisch, P., Funsten, H. O., Fuselier, S., et al. (2009). “IBEX—interstellar boundary explorer.” *Space science reviews*, 146, 11–33.
- McComas, D., Lewis, W., and Schwadron, N. (2014). “IBEX’s Enigmatic Ribbon in the sky and its many possible sources.” *Reviews of Geophysics*, 52, 1, 118–155.
- Osthus, D., Weaver, B. P., Beesley, L. J., Moran, K. R., Stricklin, M. A., Zirnstein, E. J., Janzen, P. H., and Reisenfeld, D. B. (2023). “Toward Improved Heliosphere Sky Map Estimation with Theseus.” *Technometrics*, 66, 2, 208–226.

- Rasmussen, C. E. (2003). *Gaussian processes in machine learning*. Springer.
- Roberts, S., Osborne, M., Ebden, M., Reece, S., Gibson, N., and Aigrain, S. (2013). “Gaussian processes for time-series modelling.” *Philosophical Transactions of the Royal Society A: Mathematical, Physical and Engineering Sciences*, 371, 1984, 20110550.
- Sauer, A., Cooper, A., and Gramacy, R. B. (2023). “Vecchia-approximated deep Gaussian processes for computer experiments.” *Journal of Computational and Graphical Statistics*, 32, 3, 824–837.
- Stein, M. L. (1999). *Interpolation of spatial data: some theory for kriging*. Springer Science & Business Media.
- Stuart, A. M. (2010). “Inverse problems: a Bayesian perspective.” *Acta numerica*, 19, 451–559.
- Swaczyna, P., McComas, D., Zirnstein, E., Sokół, J., Elliott, H., Bzowski, M., Kubiak, M., Richardson, J., Kowalska-Leszczynska, I., Stern, S., et al. (2020). “Density of neutral hydrogen in the sun’s interstellar neighborhood.” *The Astrophysical Journal*, 903, 1, 48.
- Vecchia, A. V. (1988). “Estimation and model identification for continuous spatial processes.” *Journal of the Royal Statistical Society Series B: Statistical Methodology*, 50, 2, 297–312.
- Wu, L., Pleiss, G., and Cunningham, J. P. (2022). “Variational nearest neighbor Gaussian process.” In *International Conference on Machine Learning*, 24114–24130. PMLR.
- Zhang, J. and Katzfuss, M. (2022). “Multi-scale Vecchia approximations of Gaussian processes.” *Journal of Agricultural, Biological and Environmental Statistics*, 27, 3, 440–460.
- Zirnstein, E., Dayeh, M., and Heerikhuisen, J. (2021a). “Dependence of the IBEX ribbon geometry on pitch-angle scattering outside the heliopause.” *The Astrophysical Journal*, 908, 1, 35.
- Zirnstein, E., Dayeh, M., Heerikhuisen, J., McComas, D., and Swaczyna, P. (2021b). “Heliosheath proton distribution in the plasma reference frame.” *The Astrophysical Journal Supplement Series*, 252, 2, 26.
- Zirnstein, E., Heerikhuisen, J., and Dayeh, M. (2018). “The role of pickup ion dynamics outside of the heliopause in the limit of weak pitch angle scattering: implications for the source of the IBEX Ribbon.” *The Astrophysical Journal*, 855, 1, 30.
- Zirnstein, E., Kumar, R., Shrestha, B., Swaczyna, P., Dayeh, M., Heerikhuisen, J., and Szalay, J. R. (2025). “Global heliospheric termination shock strength in the solar–interstellar interaction.” *Nature Astronomy*, 1–16.
- Zirnstein, E., McComas, D., Schwadron, N., Dayeh, M., Heerikhuisen, J., and Swaczyna, P. (2019). “Strong Scattering of keV Pickup Ions in the Local Interstellar Magnetic Field Draped around Our Heliosphere: Implications for the IBEX Ribbon’s Source and IMAP.” *The Astrophysical Journal*, 876, 2, 92.

A Additional empirical validation

Here we provide some supplementary results to further validate the methodology introduced in the main body of our manuscript and lay additional groundwork for future research endeavors.

A.1 Probability Integral Transforms

Section 4.2 showcased the ability of our Poisson Bayesian inverse problem framework to recover the “true” model parameters u from synthetic satellite data. In particular, we made the claim that both sky maps in Figure 9 (bottom left, top right) could have reasonably generated the ENA counts “observed” in the top left plot of that figure. This assertion was based on a purely visual assessment of the data and the estimated underlying ENA rate. A more empirical method to validate our claim could be via the probability integral transform (PIT; Gneiting et al., 2007; Diebold et al., 1997; Dawid, 1984).

PIT values, frequently visualized in PIT histograms, are used to evaluate predictions and forecasts from a statistical model. In short, the PIT compares observed data to the CDFs of predictive distributions. If observations came from the predicted distributions, PIT values should be distributed uniformly between 0 and 1. For discrete data such as our Poisson counts, PIT values will not be uniformly distributed, due to the step function nature of the CDF. A randomized PIT is used in these scenarios (Gneiting and Katzfuss, 2014; Czado et al., 2009), as we will do for the IBEX data.

Figure 15 displays PIT histograms for comparing synthetic counts to predicted ENA rates computed via a surrogate for our computer model $m(\cdot, \cdot)$ at estimated model parameter \hat{u} . To keep it short, here we show only 15 of the 36 cases from Figure 10. Titles of each plot indicate the true model parameter u^* that was used to sample the synthetic data. If the data “observed” comes from a Poisson distribution with a mean surface $\lambda(X) = \hat{m}(\hat{u}, X)$, then we’d expect the PIT histogram to be distributed evenly between 0 and 1. This is certainly the case for all 15 histograms shown. No significant departure from a Uniform(0,1) is observed. Therefore, we can add further empirical backing to our visual assessment that estimates from our framework reasonably explain the data “observed.”

In contrast to the results in Figure 9 (and more broadly in Figure 10), our Poisson Bayesian inverse problem framework struggles to estimate a value for u that produces a map of ENA rates that is likely to have generated the actual data observed from the IBEX satellite. This is due in large part to the insufficiencies of the IBEX simulator. To illustrate, consider Figure 16. Here we display PIT histograms produced by comparing IBEX satellite data to surrogate predicted sky maps using estimates of u from our framework. On the left we show results when satellite data from years 2009-2011 is used as the field data (X^F, Y^F) . On the right we show results when treating years individually from 2012-2021 as (X^F, Y^F) . These panels correspond to Figures 11 and 13, respectively.

The departure from uniformity is clear. For years 2009-2011, we get a crater-shaped histogram, indicating that the predicted ENA rate surface does not sufficiently account for the extreme observations in the satellite data. That is, the observed data fell too frequently in the tails of our predicted distribution. This is consistent with the spatially-varying discrepancy we observed in Figure 14. For years 2012-2021, we see a different, though consistent, behavior. Although individual

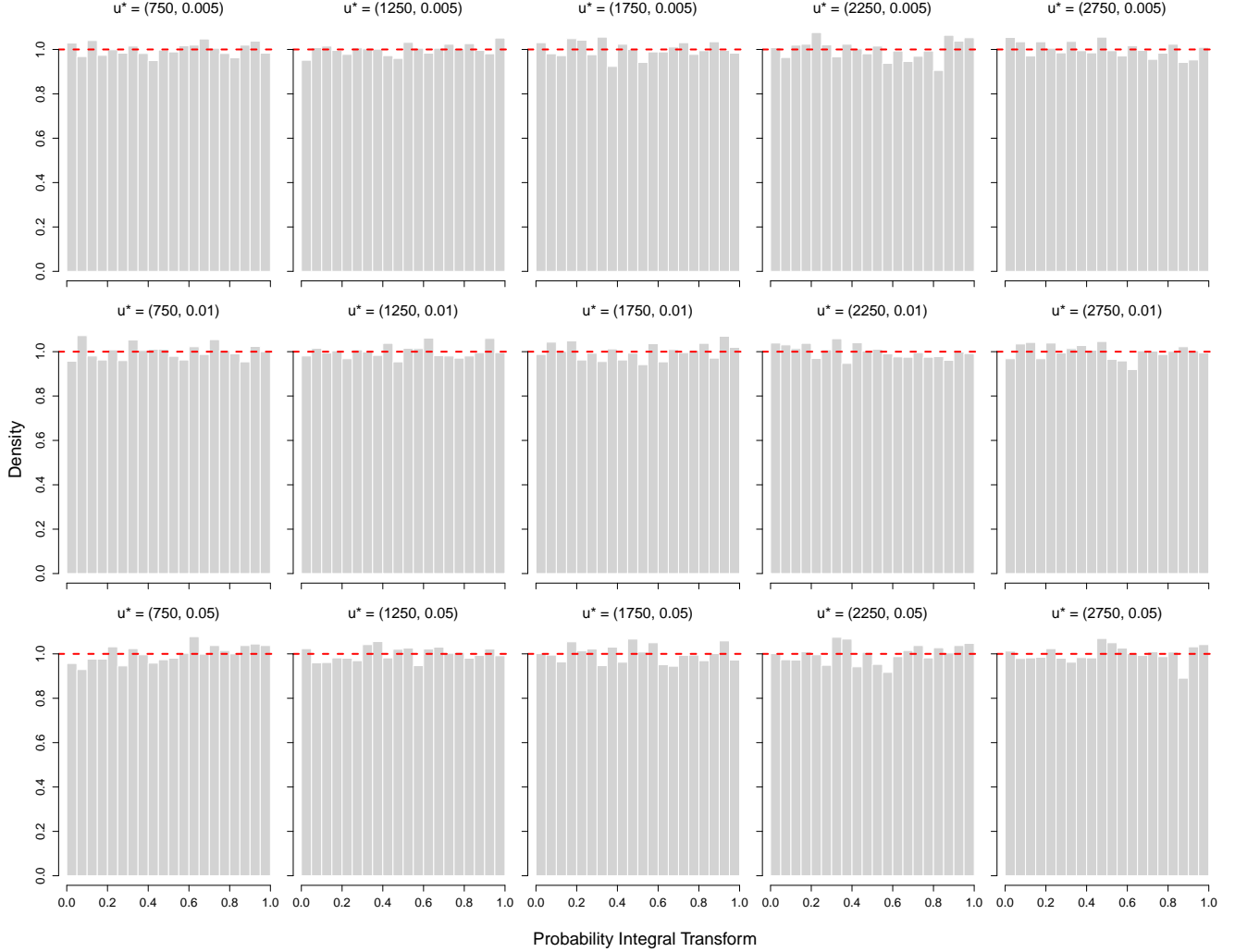


Figure 15: Probability integral transform (PIT) histograms for 15 sets of estimated sky maps and their corresponding synthetic “observed” datasets. Red dashed lines are drawn at 1 to show where we’d expect the histograms to approach as the number of draws goes to infinity.

years vary, each PIT histogram is right-skewed. This means that with the estimated u , the output from the IBEX computer model, or the surrogate fit on the simulator output, is systematically overpredicting the ENA rates for the years 2012-2021.

A.2 Multiplicative Scale Discrepancy

Equation 5 introduces a simple, multiplicative term δ in an attempt to account for the gap between the predicted ENA rates and ENA counts observed by IBEX. Unsurprisingly, we discovered that this multiplicative scale was insufficient to account for the spatially-varying, nonstationary discrepancy present in the satellite data. However, we gave no evidence to suggest that, if indeed there only existed a multiplicative discrepancy, our updated model would be able to correctly identify it.

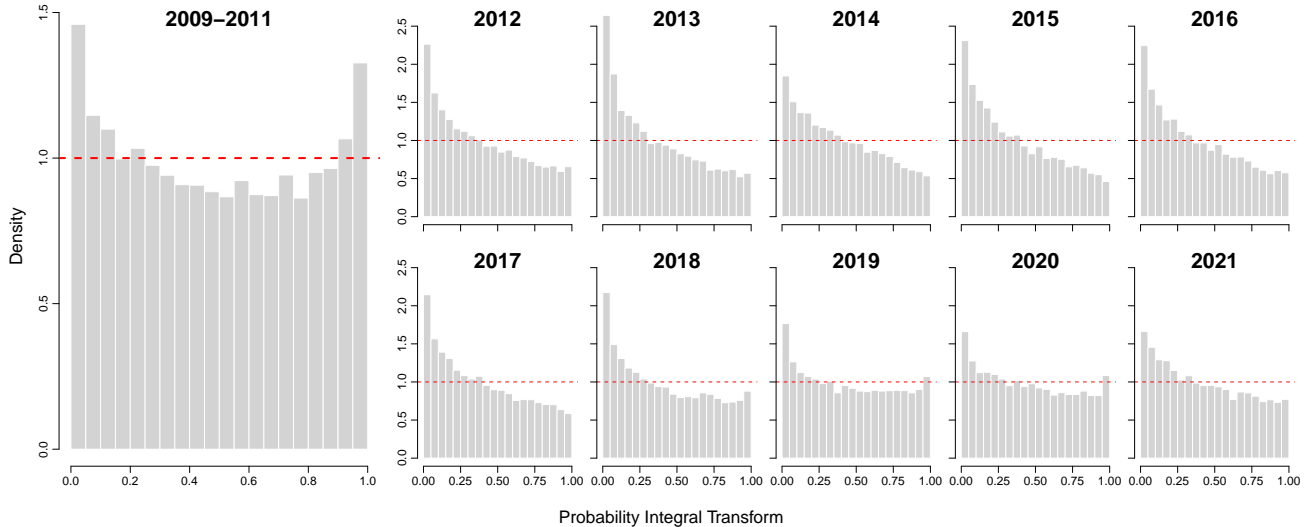


Figure 16: Probability integral transform (PIT) histograms comparing ENA counts collected by IBEX and predicted sky map from estimated model parameters. The very left panel displays the PIT histogram for estimates from combined years 2009-2011. PIT histograms for individual years 2012-2021 are shown in the two rows on the right. U-shaped PIT histograms indicate overdispersion. Right-skewed PIT histograms indicate consistent overprediction.

Therefore, in order to verify that our scale discrepancy actually works, we conducted an experiment on simulated data that fall within that model class.

First, we select one sky map from the simulator output corresponding to one of the $n = 66$ u -values and set this as λ^* . Next, we both scale λ^* by δ and add in the background rate, λ_b . Then, we generate synthetic satellite data via counts drawn from a Poisson, $Y_i^F \sim \text{Pois}(\lambda_i^* * \delta + \lambda_{b_i}, e_i)$ for given exposure times e_i . Finally, we run Algorithm 1, modified slightly to sample for a multiplicative scale discrepancy, and calculate a posterior mean and 95% credible intervals for δ . We repeat this process for 10 different values of δ .

Figure 17 shows histograms of posterior samples of δ as estimated densities. We restrict the y -axis limits to be the same, which causes different bar heights among the plots due to the variation in spread of the posterior samples on the x -axes. In each of the 10 test cases, our framework is able to recover the true value of δ . Although not shown here, it's important to mention that in addition to successfully estimating δ , our framework also recovered the true u -values used to generate the synthetic data at the nominal 95% rate. Therefore, we can be confident that had the disparity between the IBEX simulator and the IBEX satellite data been in the form of a multiplicative scale, our method would be able to identify it. Alas, we look forward to future work exploring more sophisticated discrepancy models and better capturing the mismatch between simulator and reality.

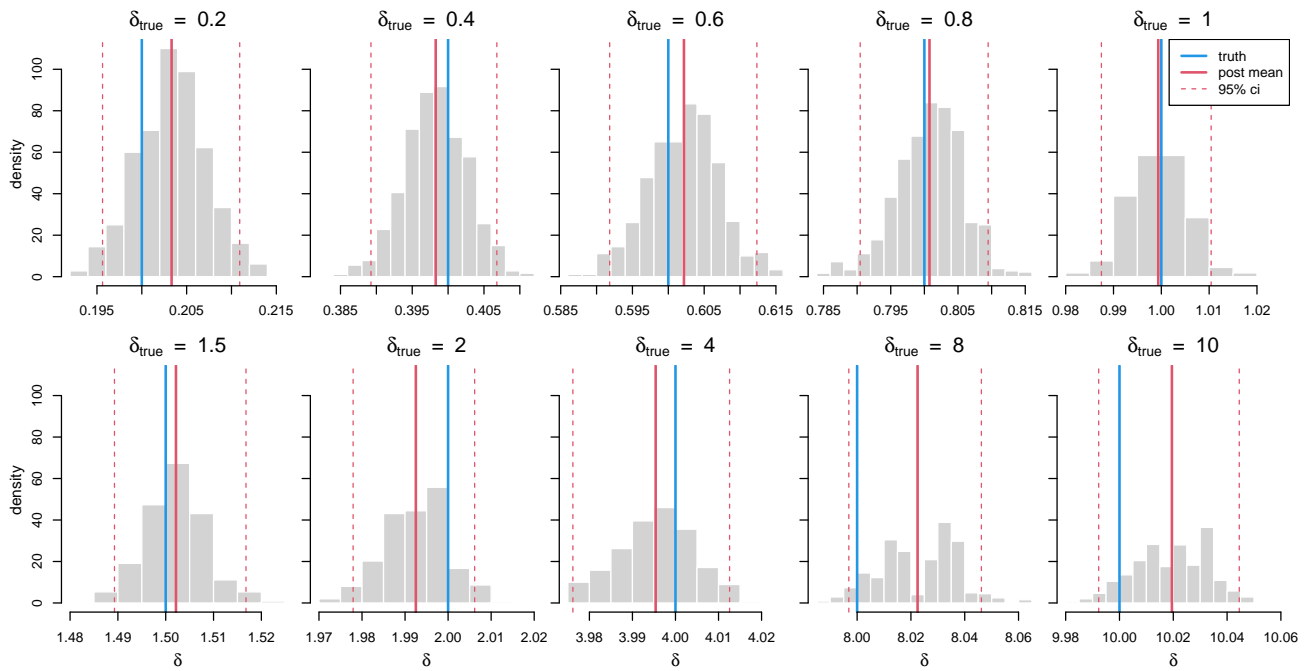


Figure 17: Posterior samples of a multiplicative scale discrepancy, δ . Each panel corresponds to a Metropolis sampler run on synthetic data artificially scaled by separate known constants (δ_{true}). True values marked in blue. Posterior means and 95% credible intervals shown in red.